Coarse-grained local and objective continuum description of three-dimensional granular flows down an inclined surface

Thomas Weinhart, Remco Hartkamp, Anthony R. Thornton, and Stefan Luding

Citation: Physics of Fluids (1994-present) **25**, 070605 (2013); doi: 10.1063/1.4812809
View online: http://dx.doi.org/10.1063/1.4812809
View Table of Contents: http://scitation.aip.org/content/aip/journal/pof2/25/7?ver=pdfcov
Published by the AIP Publishing

PHYSICS OF FLUIDS **25**, 070605 (2013)

Coarse-grained local and objective continuum description of three-dimensional granular flows down an inclined surface

Thomas Weinhart,[1,a)] Remco Hartkamp,[1,b)] Anthony R. Thornton,[1,2,c)] and Stefan Luding[1,d)]
[1]*Multi Scale Mechanics, CTW and MESA+, University of Twente, P.O. Box 217, 7500AE Enschede, The Netherlands*
[2]*Mathematics of Computational Science, EWI, University of Twente, P.O. Box 217, 7500AE Enschede, The Netherlands*

(Received 10 September 2012; accepted 15 April 2013; published online 18 July 2013)

Dry, frictional, steady-state granular flows down an inclined, rough surface are studied with discrete particle simulations. From this exemplary flow situation, macroscopic fields, consistent with the conservation laws of continuum theory, are obtained from microscopic data by time-averaging and spatial smoothing (coarse-graining). Two distinct coarse-graining length scale ranges are identified, where the fields are almost independent of the smoothing length w. The smaller, sub-particle length scale, $w \ll d$, resolves layers in the flow near the base boundary that cause oscillations in the macroscopic fields. The larger, particle length scale, $w \approx d$, leads to smooth stress and density fields, but the kinetic stress becomes scale-dependent; however, this scale-dependence can be quantified and removed. The macroscopic fields involve density, velocity, granular temperature, as well as strain-rate, stress, and fabric (structure) tensors. Due to the plane strain flow, each tensor can be expressed in an inherently anisotropic form with only four objective, coordinate frame invariant variables. For example, the stress is decomposed as: (i) the isotropic pressure, (ii) the "anisotropy" of the deviatoric stress, i.e., the ratio of deviatoric stress (norm) and pressure, (iii) the anisotropic stress distribution between the principal directions, and (iv) the orientation of its eigensystem. The strain rate tensor sets the reference system, and each objective stress (and fabric) variable can then be related, via discrete particle simulations, to the inertial number, I. This represents the plane strain special case of a general, local, and objective constitutive model. The resulting model is compared to existing theories and clearly displays small, but significant deviations from more simplified theories in all variables – on both the different length scales.
 [http://dx.doi.org/10.1063/1.4812809]

I. INTRODUCTION

Granular flows display many interesting phenomena that can also be found in colloidal systems or complex fluids. However, often Brownian motion and temperature can be ignored, while diverse modes of energy dissipation, e.g., friction or plastic deformations allow for non-equilibrium steady state situations. Even though, (dilute and moderately dense) collisional flows can be well described by kinetic theory,[1] see, e.g., Ref. 2 for the inclined flow case. There is no closed theoretical framework or rheological model available yet that also includes the possible co-existence of rapid, intermediate,

[a)]t.weinhart@utwente.nl. URL: http://www2.msm.ctw.utwente.nl/weinhartt/
[b)]hartkamp@mit.edu
[c)]a.r.thornton@utwente.nl
[d)]s.luding@utwente.nl

inertial and slow, quasi-static, or even stagnant regimes under general flow conditions. However, some promising approaches have recently been proposed, such as Refs. 3–8 and references therein.

The goal of this study is to generalize/extend existing theories based on observations made from discrete particle simulations of frictional avalanching flows in plane strain steady state situations.

A rheological model is formulated using (objective) invariants of the tensors and thus is not restricted to this particular special case. Here, however, we choose a particular coordinate system with flow along the x-axis, varying along height, z, and homogeneous in the perpendicular direction, y.

A. Granular flows overview

Granular avalanche flows are a representative example and common in natural environments and industrial processes. They can differ in size by many orders of magnitude. Examples range from rock slides, containing upwards of 1000 m^3 of material; to the flow of sinter, pellets, and coke into a blast furnace for iron-ore melting; down to the flow of fine sand in an hour-glass. The dynamics of these flows are influenced by many factors such as: polydispersity, variations in density, non-uniform particle shape, complex basal topography, surface contact properties, coexistence of static, steadily flowing, and accelerating material, and flow around obstacles and constrictions.

The discrete particle method (DPM), also known as discrete element method, is closely related to molecular dynamics. It is an extremely powerful tool to investigate phenomena on the discrete particle and contact scale. With the rapid improvement in computational power, the simulation of flows containing millions of particles is now feasible. DPM simulations provide insight in the microscopic origins of global, larger scale, macroscopic mechanisms; most of the rich phenomenology can be studied with simple systems of spheres. Furthermore, via coarse-graining, local macroscopic quantities, such as density, strain rate, stress, and structure (fabric) can be extracted relatively easily from the discrete simulation data (particle positions, velocities, as well as interaction forces and torques).[9]

Various simulations and experiments have been performed on confined (granular) flows with the aim to understand and describe their flow behavior by identifying the relevant global and local physical quantities.

B. Flow modeling overview

A widely accepted basic rheological model for granular flows – in the dense, quasi-static, and inertial regimes – is the so-called $\mu(I)$-rheology.[10–13] Many experimental and numerical studies suggest that the mass density ρ and the macroscopic (bulk) friction μ are functions of the inertial number,

$$I = \dot{\gamma} d \sqrt{\rho_p / p}, \tag{1}$$

where $\dot{\gamma}$ is the shear rate, d the particle diameter, ρ_p the particle density, and p the (compressive) pressure. Alternative definitions of the inertial number often use the confining stress σ_{zz}, instead of the objective first invariant, i.e., the pressure p; however, σ_{zz} is only then an objective variable, if it is properly defined perpendicular to the flow direction, as can be done for plane strain shear flows, but not for more general deformation modes.[5] On the other hand, under the often used isotropy assumption, $p = \sigma_{zz}$, the difference in definitions of I is hidden, but will be unraveled in this study.[14] Since the strain rate tensor defines the reference system, the macroscopic fields and the involved constitutive models that describe the flow are then expressed as functions of the scalar I, which is the only objective strain rate measure. The inertial number can be interpreted as the ratio of two time scales, the pressure-induced inertial time scale $\tau_p = d\sqrt{\rho_p / p}$, and the time scale of deformation, i.e., the inverse strain rate, $\tau_\gamma = \dot{\gamma}^{-1}$. This allows the classification of slow, quasi-static flows as those with $I \ll 1$, when the deformation is much slower than typical inertial relaxation. While this simple $\mu(I)$-model can predict the flow astonishingly well, it is neither perfect in the quantitative sense, nor is it qualitatively accurate near the basal and surface boundaries.[12] Various non-local granular stress rheology models[3,4,15,16] have been proposed that are able to reproduce some of the

boundary and correlation effects. All of these models remain in spirit scalar and do not contain other time-scales[8,17] or any relation to the anisotropic structure of the material,[5,7,18] which is particularly pronounced close to the flat walls.

A further question is if continuum theories can be developed at all for granular flows, as they exhibit complex behavior such as force chains and slow cage breaking. To answer this question, Rycroft *et al.*[19] studied small representative volume elements in silo and shear flow situations. Their results suggest that reasonable continuum interpretations are possible. Among their findings was that while the instantaneous stress-strain tensor was strongly non-collinear (stress and strain eigendirections deviated by up to 15°), the non-collinearity decreased significantly when the data were time-averaged.

In the following, like the majority of material/flow models, we use the assumption that the stress tensor is symmetric in steady state flow, since non-symmetry of stress would lead to micro-polar or Cosserat-type theories,[20,21] which go far beyond the scope of this research. Various models make additional assumptions that are only valid in certain limits, but can lead to very elegant and useful constitutive relations, e.g., classical elasticity theory, the physics of Newtonian fluids, or the $\mu(I)$-rheology introduced above. Examples of simplifying assumptions that do not hold for general granular flow situations are (i) isotropy (of stress and/or structure), (ii) a linear relation between stress and strain (rate), (iii) collinearity of stress and strain (rate), and (iv) associated flow.[21,22]

C. Anisotropy of stress and structure

However, anisotropy, as often quantified by normal stress differences, has been predicted and consistently and repeatedly been observed in simulations, theories, and experiments of sheared flows of complex fluids and granular media, contradicting assumption (i).[23] Assumption (ii) does not hold in so-called yield-stress fluids as well as in granular materials, which both include fluid- and solid-like behavior ($\mu(I \to 0) > 0$). For large strain rates and non-symmetric velocity gradients, one can observe non-collinear stress-strain (rate) relations,[19,24,25] which makes assumption (iii) problematic. Furthermore, non-associated flow rules are better suited for many realistic granular materials, such as soils, which renders (iv) also invalid for this type of flow.[20,21]

In granular systems, one advantage is that the structure and even the stress tensor can be experimentally observed with relatively little effort, so that the notion of a fabric tensor is not only supported by numerical simulations but also by many experiments, as in Ref. 26 and references therein. The most recent studies from the granular community that involve constitutive relations for stress and fabric support the notion of a structure (fabric) that evolves differently from the stress.[5,7,18]

In the much older field of (sheared) complex fluids, qualitatively similar anisotropies have been observed previously for both (structure) fabric and stress tensors. Clark and Ackerson[27] were the first to experimentally observe shear-induced distortion of a suspension of interacting colloidal particles, i.e., a difference between the principal orientation of the fabric and the strain rate tensor. Shortly after, Hess and Hanley[28–31] derived a tensorial expansion for the pair correlation function to a tensor of rank 2, also referred to as the anisotropy tensor. Furthermore, a differential (evolution) equation was presented that related the coefficients of the expansion to a phenomenological relaxation time of the fluid, and showed a rotation of the structure tensor with respect to the strain rate tensor.

Since stress anisotropy is often classified in terms of the normal stress differences, those are reviewed in the following. Large-scale geophysical granular flows are often modeled using a depth-averaged framework, see, e.g., Savage and Hutter.[32] One of their key predictions is a positive first stress difference for granular avalanches. For a sheared system with flow in the x-direction, varying with height z, the velocity gradient $\nabla\mathbf{V} = \dot{\gamma}(z)\mathbf{xz}$, with respective unit-vectors $\mathbf{x}$ and $\mathbf{z}$, we denote the first (scaled) normal stress difference (between the direction of the velocity and its variation) as $\mathcal{N}_1 = (\sigma_{xx} - \sigma_{zz})/p$, with $\boldsymbol{\sigma}$ the compressive stress. The second (scaled) normal stress difference involves the normal stress in the third, "neutral" direction and is defined as $\mathcal{N}_2 = (\sigma_{zz} - \sigma_{yy})/p$.

In 1998, Sela and Goldhirsch[1] developed closure relations for rapid flows of smooth inelastic spheres. They used the Chapman-Enskog expansion to develop hydrodynamic equations to Burnett order, predicting a positive first and second normal stress difference, while Jin and Slemrod[33] regularized this model to remove unphysical instabilities. This model was generalized by Alam

and Luding[34,35] to explain the normal stress differences, which changed sign in their simulations, of uniform two-dimensional shear flow simulations. The first normal stress difference was positive for dilute flows and slightly negative for very dense flows. A positive first normal stress difference has also been observed in dense (three-dimensional) suspensions,[36,37] where the second normal stress difference was reported to exceed the first. We follow the ideas of Alam and Luding,[35] who observed from simulations, and modeled theoretically, both positive and negative first normal stress differences (in 2D), and Hartkamp *et al.*[38] who observed stress anisotropy in molecular flow through nano-channels that extends further than the layering of density into the bulk of the Lennard-Jones fluid. Such density oscillations near the surface, a phenomenon already recently reviewed,[39] will also be shown here, but do not (yet) form an ingredient of the model.

D. Motivation of this study

In summary, this paper aims to (i) to provide a description of the full stress tensor for sheared planar flow, decomposed into state variables describing the non-Newtonian stress components. Since the model is supposed to work in all situations, we choose to express these variables in terms of their objective, frame-invariant quantities, and not in components that are specific to the choice of the (e.g., Cartesian) coordinate system, as is the natural choice for chute flow simulations. Which tensor invariants are used is not important, since eigenvalues or other invariants, can all be related to each other – and also to the Cartesian components – as will be shown at the end of this study. The second objective is to (ii) observe and quantify the state variables as functions of the governing control parameter(s), which is (only) the inertial number I for dense, quasistatic, inertial granular flows. We expect to observe significant differences from the simplifying assumptions outlined in Sec. I B, such as the non-collinearity of stress, fabric, and strain rate, and the anisotropy, or shape, of the tensors, both in the flow plane and perpendicular to it. Finally, we will (iii) look at the relation between the stress and the fabric, or structure tensor, which might allow us to determine the micro-structural causes of the stress anisotropy and non-Newtonian behavior.

The paper is organized as follows: Sec. II gives a description of the system and the simulation method. In Sec. III, the calculations of microscopic and macroscopic fields are presented. In Sec. IV, tensors are expressed in terms of their invariants and orientations with the goal to formulate an objective, generally applicable, local constitutive model. In Sec. V, the results of various simulations are shown and analyzed. In Sec. VI, the relation between variables of the constitutive model and the measured microscopic and macroscopic fields are studied. Finally, in Sec. VII, the results are summarized and discussed.

II. SYSTEM DESCRIPTION

A discrete particle method is used to investigate granular chute flows as an exemplary case, in the steady, continuous flow regime. We use a coordinate system where x denotes the flow direction, y the in-plane vorticity direction, and z the depth direction normal to the base. The chute is inclined at an angle θ such that gravity acts in the direction $(\sin\theta,\ 0,\ -\cos\theta)$. The simulation cell has dimensions $l_x' \times l_y' = 20\,d' \times 10\,d'$ particle diameters in the (periodic) x- and y-directions (primes indicate dimensional parameters). Here, all particles are mono-dispersed with the same diameter d'. The base of the system is a rough surface consisting of N_b fixed particles, see Figure 1. N flowing particles are introduced to the system at random non-overlapping positions well above the base. Due to gravity they fall and accelerate down the slope until they reach a steady state, which is then analyzed. This system, its flow states, and a closure for a shallow-layer continuum model were described in more detail by Weinhart *et al.*[39,60]

We use a linear elastic-dissipative normal force model with frictional forces in tangential direction.[39,40] The parameters of the system are non-dimensionalized such that the particle diameter is $d = 1$, their mass is $m = 1$, and the magnitude of gravity is $g = 1$. Therefore, the particle density, in our units, is $\rho_p = m/\mathcal{V} = 6/\pi$, with particle volume $\mathcal{V} = \pi d^3/6$. The (dimensionless) normal spring and damping constants are $k^n = 2 \times 10^5$ and $\gamma^n = 50$, respectively; thus, the collision time (contact duration for pair collisions) is $t_c = 0.005$ and the coefficient of restitution is $e_n = 0.88$. The

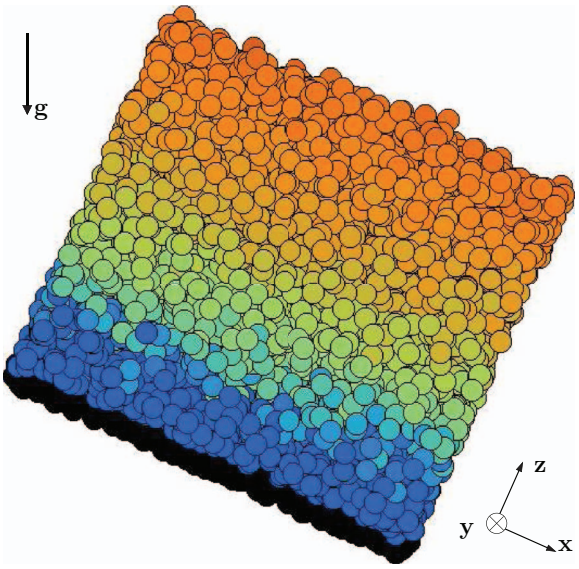

FIG. 1. DPM simulation for $N = 3500$ and inclination $\theta = 24^\circ$ at time $t = 2000$; gravity direction $\mathbf{g}$ as indicated. The domain is periodic in x- and y-directions. In the z-direction, fixed particles (black) form a rough base while the surface is unconstrained. Shades/colors indicate speed, from darkest gray (blue) through light gray (green/yellow) to mid-gray (orange) as z increases.

tangential spring and damping constants are $k^t = (2/7)k^n$ and $\gamma^t = \gamma^n$, such that the frequency of normal and tangential contact oscillation are similar, and the normal and tangential dissipation are comparable. The microscopic friction coefficient is set to $\mu_c = 0.5$.

The interaction parameters are chosen as in Silbert *et al.*[41] to simulate glass particles of diameter $d' = 0.1$ mm, which thus represents the unit/dimension of length; using $g' = 9.8$ m s^{-2}, this fixes the dimensional time scale as $t' = \sqrt{d'/g'} = 3.2$ ms, so that $t'_c = t't_c = 16$ μs, i.e., $t_c = 0.005$, and the dimensional velocity scale is $v' = \sqrt{d'g'} = 0.031$ m s^{-1}. Finally, with the density of glass $\rho'_p = 2500$ kg m^{-3}, this sets the unit of mass as $m' = \rho'_p \frac{\pi}{6} d'^3 = 1.3 \times 10^{-9}$ kg. In the rest of the paper, we will use the dimensionless units, but the examples in this paragraph show how to translate between dimensionless and dimensional values.

We integrate the resulting force and torque equations of motion for all particles in time using the Velocity-Verlet and Euler algorithms, respectively, with a time step $\Delta t = t_c/50$. The system is integrated between $t \in [0, 2000]$ to allow the system to reach a steady state. The range of steady states was described in detail in Weinhart *et al.*[39] Steady states exist for inclinations $\theta_{stop} \le \theta \le \theta_{acc}$, where

$$\tan\theta_{stop} = \tan\theta_1^{stop} + \frac{\tan\theta_2^{stop} - \tan\theta_1^{stop}}{h/(Ad) + 1}, \quad \theta_{acc} = 29^\circ \pm 1^\circ, \tag{2}$$

with $\theta_1^{stop} = 17.6^\circ$, $\theta_2^{stop} = 32.3^\circ$, and $A = 3.84$. To study a wide range of steady flow regimes, simulations are performed for inclinations θ varying between 20° and 28° and for different numbers of flowing particles $N = 2000, 4000, 6000$, and 8000.

In the following, various different steady state shear flow data sets, in the regime specified above, will be studied and coarse grained to yield many macroscopic information (density ρ, velocity $\mathbf{V}$, stress $\boldsymbol{\sigma}$, etc.) at various heights and thus in many local flow situations. The coarse-graining procedure is explained next.

III. STATISTICS

To extract the macroscopic fields, we use the spatial coarse-graining approach as in Weinhart *et al.*,[9] and references therein, which will be reviewed in this section. It has the following advantages as compared to other simpler methods: (i) the resulting fields automatically satisfy *exactly* the

equations of continuum mechanics, even near the flow base, if the interaction with the boundary is taken into account, as proposed by Weinhart *et al.*;[39] (ii) it is not assumed that the particles are spherical (but a single point of contact is required); and (iii) the results are valid even for single particles and at one moment in time; no ensemble averaging is required. Here, however, we apply long-time averaging over a single realization.

A. Mass density and velocity

It is assumed that each particle's mass is located at its center and that collisions are not instantaneous (i.e., soft). Furthermore, each particle pair has a single point of contact (i.e., the particle shapes are convex), and the contact area can be replaced by a contact point (i.e., the particles are not too soft). Flow particles are labeled from 1 to N, while boundary particles are labeled from $N+1$ to $N+N_b$.

From statistical mechanics, the microscopic (point) mass density of the flow, ρ^{mic}, at a point $\mathbf{r}$ at time t is defined by

$$\rho^{\mathrm{mic}}(\mathbf{r},t)=\sum_{i=1}^{N} m\delta\left(\mathbf{r}-\mathbf{r}_i(t)\right), \tag{3}$$

where $\delta(\mathbf{r})$ is the Dirac delta function.

A macroscopic mass density field can then be extracted by convoluting the microscopic mass density with a coarse-graining function $\mathcal{W}(\mathbf{r})$, which yields

$$\rho(\mathbf{r},t)=\sum_{i=1}^{N} m\int_{\mathbb{R}^3}\delta\left(\mathbf{r}'-\mathbf{r}_i(t)\right)\mathcal{W}\left(\mathbf{r}-\mathbf{r}'\right)d\mathbf{r}'=\sum_{i=1}^{N} m\mathcal{W}\left(\mathbf{r}-\mathbf{r}_i(t)\right). \tag{4}$$

A Lucy function[42] is used for coarse graining, which for three spatial dimensions is

$$\mathcal{W}(\mathbf{r})=\frac{105}{16\pi c^3}\left(-3\left(r/c\right)^4+8\left(r/c\right)^3-6\left(r/c\right)^2+1\right),\ \text{if } r:=|\mathbf{r}|<c,\ 0\ \text{else}, \tag{5}$$

with c the range and $w=c/2$ the half-width, or standard deviation.[43] This function has two continuous derivatives everywhere and satisfies $\int_{\mathbb{R}^3}\mathcal{W}(\mathbf{r})\,d\mathbf{r}=1$. Other coarse-graining functions are possible, but the Lucy function has the advantage that it produces twice differentiable fields and has compact support. In contrast, common compactly supported coarse-graining functions such as the Heaviside function or a cut-off Gaussian function do not have smooth gradients everywhere, whereas using a Gaussian function without a cut-off radius would be computationally expensive due to its infinite range. Furthermore, the polynomial form allows us to differentiate and integrate the function analytically, and thus to exactly evaluate spatial averages and gradients of the resulting fields. The resulting coarse-grained fields depend only weakly on the choice of the coarse-graining function, but the width w is the key parameter,[44] as will be shown later.

We define the volume fraction as

$$\nu(\mathbf{r},t)=\frac{\rho(\mathbf{r},t)}{\rho_p}=\sum_{i=1}^{N}\mathcal{V}\mathcal{W}\left(\mathbf{r}-\mathbf{r}_i(t)\right), \tag{6}$$

with $\mathcal{V}=\frac{\pi}{6}d^3$ the (constant) particle volume.

The coarse-grained momentum density vector $\mathbf{j}(\mathbf{r},t)$ has the components

$$\mathbf{j}(\mathbf{r},t)=\sum_{i=1}^{N} m\mathbf{v}_i\mathcal{W}(\mathbf{r}-\mathbf{r}_i), \tag{7}$$

where $\mathbf{v}_i$ is the velocity of particle i. The macroscopic velocity field $\mathbf{V}(\mathbf{r},t)$ is then defined as the ratio of momentum density and density fields,

$$\mathbf{V}(\mathbf{r},t)=\mathbf{j}(\mathbf{r},t)/\rho(\mathbf{r},t). \tag{8}$$

Density and momentum density exactly fulfill the continuity equation, $\frac{\partial \rho}{\partial t} + \nabla \cdot (\rho \mathbf{V}) = 0$.[9,44] The velocity gradient can now be obtained from the velocity field by a central difference approximation, see (38), or by averaging the strain rate tensor or displacement gradient tensor, as described in Refs. 38 and 45.

B. Stress

Next, we consider the momentum conservation equation with the aim of establishing the macroscopic stress tensor, $\boldsymbol{\sigma}$. As we have only repulsive forces, we use the compressive stress convention such that (compression) pressure is positive. Since we want to describe boundary stresses as well as internal stresses, the boundary interaction force density, or surface traction density, $\mathbf{t}$, has been included, as well as the gravitational force density, $\rho \mathbf{g}$, as described in detail in Weinhart *et al.*[9] The momentum balance equations then take the form

$$\frac{\partial \mathbf{j}}{\partial t} = -\nabla \cdot [\rho \mathbf{V}\mathbf{V}] - \nabla \cdot \boldsymbol{\sigma} + \mathbf{t} + \rho \mathbf{g}, \tag{9}$$

where $\mathbf{V}\mathbf{V}$ denotes the tensor (dyadic) product of two velocity vectors. We split the stress into its kinetic and contact contributions,

$$\boldsymbol{\sigma} = \boldsymbol{\sigma}^k + \boldsymbol{\sigma}^c, \tag{10a}$$

from which the (hydrostatic, isotropic) pressure is defined as

$$p(\mathbf{r}, t) = \mathrm{tr}(\boldsymbol{\sigma}(\mathbf{r}, t))/3. \tag{10b}$$

The kinetic and contact stress is defined as

$$\boldsymbol{\sigma}^k = \sum_{i=1}^{N} m \mathbf{v}_i' \mathbf{v}_i' \mathcal{W}(\mathbf{r} - \mathbf{r}_i), \tag{10c}$$

$$\boldsymbol{\sigma}^c = \sum_{i=1}^{N} \sum_{j=i+1}^{N} \mathbf{f}_{ij} \mathbf{r}_{ij} \int_0^1 \mathcal{W}(\mathbf{r} - \mathbf{r}_i + s\mathbf{r}_{ij})\, \mathrm{d}s \tag{10d}$$

$$+ \sum_{i=1}^{N} \sum_{k=N+1}^{N+N_b} \mathbf{f}_{ik} \mathbf{a}_{ik} \int_0^1 \mathcal{W}(\mathbf{r} - \mathbf{r}_i + s\mathbf{a}_{ik})\, \mathrm{d}s, \tag{10e}$$

with interaction forces $\mathbf{f}_{ij} = -\mathbf{f}_{ji}$, branch vectors $\mathbf{r}_{ij} = \mathbf{r}_i - \mathbf{r}_j$, and contact-to-center vectors $\mathbf{a}_{ik} = \mathbf{r}_i - \mathbf{c}_{ik}$, where $\mathbf{c}_{ik}$ denotes the contact point between the fluid particle i and wall particle k. Further,

$$\mathbf{v}_i'(\mathbf{r}, t) = \mathbf{v}_i(t) - \mathbf{V}(\mathbf{r}, t) \tag{11}$$

is the fluctuation velocity of particle i, which leads to scale dependency effects as discussed below in Subsection V A. The boundary interaction force density

$$\mathbf{t} = \sum_{i=1}^{N} \sum_{k=N+1}^{N+N_b} \mathbf{f}_{ik} \mathcal{W}(\mathbf{r} - \mathbf{c}_{ik}) \tag{12}$$

is applied by the base to the flow and has nonzero values only near the basal surface. It can be introduced into continuum models as a boundary condition for the stress

$$\sigma_{\alpha z}(z = b) = \int_{\mathbb{R}} t_\alpha(z)\, dz, \text{ for } \alpha = x, y, z. \tag{13}$$

For the chute flows presented here, $\sigma_{zz}(z = b) = -Nmg \cos\theta/(l_x l_y)$, as will be discussed further in Subsection V B.

C. Temperature and fabric

Further terms can be defined that are not part of traditional stress-strain constitutive relations. The so-called granular temperature is a measure of the squared fluctuation velocities that can be obtained by scaling the kinetic fluctuation energy density (twice per particle per degree of freedom per mass),

$$T_g = \frac{\mathrm{tr}(\boldsymbol{\sigma}^k)}{3\rho}, \tag{14}$$

but one can also use $T_B = \frac{\mathrm{tr}(\boldsymbol{\sigma}^k)}{3n}$, with number density $n = \rho/m$, equivalent to the thermodynamic temperature $k_B T_B$ used in atomistic simulations.

The fabric, or structure tensor, is an approximate macroscopic measure of the contact orientation distribution, and is defined by

$$\begin{aligned}\mathbf{F} = &\sum_{i=1}^{N}\sum_{j=1,j\neq i}^{N} \mathcal{V}\mathbf{n}_{ij}\mathbf{n}_{ij}\int_0^1 \mathcal{W}(\mathbf{r}-\mathbf{r}_i+s\mathbf{r}_{ij})\,\mathrm{d}s \\ &+\sum_{i=1}^{N}\sum_{k=N+1}^{N+N_b} \mathcal{V}\mathbf{n}_{ik}\mathbf{n}_{ik}\int_0^1 \mathcal{W}(\mathbf{r}-\mathbf{r}_i+s\mathbf{a}_{ik})\,\mathrm{d}s,\end{aligned} \tag{15}$$

with the contact normal unit vector $\mathbf{n}_{ij} = \mathbf{r}_{ij}/|\mathbf{r}_{ij}|$.

The trace of the fabric is its isotropic invariant and it is proportional to the contact number density,[46,47] with prefactor $g_3 = 1$ for monodisperse, (quasi-)static packings. This leads to the coordination number,

$$Z = \mathrm{tr}(\mathbf{F})/\nu, \tag{16}$$

and the corrected coordination number, $Z^* = Z(1-\phi_r)$, which excludes the volume fraction ϕ_r of particles that are so-called rattlers and thus do not contribute to a mechanically stable contact-network. Since we consider inertial flow in the following, we will use Z and not Z^* that is more relevant for static and quasi-static situations. The coordination number Z is related to the contact/collision rate from kinetic theory $f_c \propto Z/t_c$ in the collisional regime. However, this regime will not be discussed further and we refer the reader to the recent work by Jenkins and Berzi;[2] in the following, we will mostly ignore the dilute, collisional layer at the top of our chute simulations.

D. Summary of the coarse grained fields

After coarse graining, in the special steady chute-flow situation chosen, all fields are averaged over x- and y-directions and in time, which yields data at various different z-locations. Whether these data can be considered local and if there are regimes of coarse-graining widths w that yield w-independent data will be discussed in Sec. V.

From one single simulation, due to the inhomogeneous depth profiles, the data already include a set of different local flow states that can be processed and studied further. The fields involve scalar (isotropic) variables ρ, T_g, Z, vectors $\mathbf{V}$, and tensors $\nabla\mathbf{V}$, $\boldsymbol{\sigma}$, $\mathbf{F}$ that are not all independent from each other. Their behavior and relations for different flow conditions will be discussed in Sec. V, after the tensor- and constitutive relations are introduced in Sec. IV.

IV. OBJECTIVE VARIABLES FOR CONSTITUTIVE MODELS

In the following, the goal is to introduce a local, objective decomposition of the tensor variables to formulate the constitutive model with anisotropic stress. The model is similar to the one proposed by Hartkamp *et al.*[38] for 3D molecular fluids and is based on observations and ideas of Alam and Luding[35] concerning the change of the sign of the first normal stress difference for high densities. Particular for such a model is that the orientations of the stress and strain tensors are (allowed to be) variables.

A. Example: Objective velocity gradient decomposition

Here, we recall basic tensor algebra using as example the velocity gradient.[48] In general flow situations, every tensor, as for example the velocity gradient, can be split into its isotropic, deviatoric (symmetric, trace-free) and anti-symmetric contributions,

$$\nabla \mathbf{V} = \dot{\epsilon}_v \mathbf{1} + \mathbf{S}_D + \mathbf{W}, \tag{17}$$

where $\mathbf{1}$ is the identity tensor. The isotropic average strain rate, $3\dot{\epsilon}_v := \mathrm{tr}(\nabla \mathbf{V})$, accounts for volume changes; the deviatoric strain rate,

$$\mathbf{S}^D := \frac{1}{2}\left(\nabla \mathbf{V} + (\nabla \mathbf{V})^{\mathrm{T}}\right) - \dot{\epsilon}_v \mathbf{1}\,, \tag{18}$$

accounts for (isochoric) shape changes; and the antisymmetric strain rate, the vorticity tensor,

$$\mathbf{W} := \frac{1}{2}\left(\nabla \mathbf{V} - (\nabla \mathbf{V})^{\mathrm{T}}\right), \tag{19}$$

quantifies the "continuum rotation," i.e., the vorticity of the flow.

In general, every tensor can be expressed by its components according to, e.g., a Cartesian coordinate system that is chosen based on a certain flow situation or experimental geometry. In this study, the chute flow suggests to use x, y, z in flow-, vorticity-, and height-directions, respectively. However, every tensor can also be expressed (re-written, without loss of information) by its invariants and eigendirections. This keeps the tensor general, objective (coordinate frame independent), and allows one to focus on the variables with physical meaning and the directions separately.

The velocity gradient has 9 independent components and when expressed in its (symmetric) invariants (3 components) and eigendirections (3 components), there remains a vorticity vector (3 components). From the symmetric part, when extracting the isotropic part, two deviatoric invariants and the eigendirections, $\boldsymbol{\epsilon}_i$, remain. While there is not much choice for the isotropic strain rate and the vorticity vector, the deviatoric strain rate tensor invariants can now be chosen, e.g., as $\dot{\epsilon}^D := J_2^S = (1/\sqrt{6})\sqrt{(S_1^D - S_2^D)^2 + (S_1^D - S_3^D)^2 + (S_2^D - S_3^D)^2}$, and $J_3^S = S_1^D S_2^D S_3^D$ or, without loss of generality, as the first two eigenvalues S_1^D and S_2^D, or any other combination thereof that describe the "shape" of the (deviatoric) tensor as, e.g., S_1^D and $\xi_S = S_2^D/S_1^D$, since only two are independent.[49] The sorting convention $S_1^D \leq S_2^D \leq S_3^D$ is implied, which means that $S_1^D < 0$ is the eigenvalue that corresponds to the eigendirection with the strongest compressive strain rate. This exercise will be carried out without much explanation also for the other tensors below, but for stress and fabric, the largest eigenvalue will be assigned as the first. When considering the negative strain rate, all sorting conventions would be identical.

For chute flow in steady state, when choosing the coordinate system as defined before, the velocity gradient takes a very simple form, since all components vanish, except $\dot{\gamma} = \partial V_x/\partial z \neq 0$. The invariant, objective representation is then $\dot{\epsilon}^D = \dot{\gamma}$ and $\xi_S = 0$ (therefore $S_1^D = -S_3^D = -\dot{\gamma}/2$, and $S_2^D = 0$), and the vorticity vector $\boldsymbol{\omega} = (1/2)\nabla \times \mathbf{V} = (\dot{\gamma}/2)\mathbf{y}$ quantifying the vorticity in positive y-direction, which is associated to the vorticity tensor $\mathbf{W}$. The eigendirections will be discussed and given below. Note that due to the choice of the specific chute flow geometry and the steady flow situation, one has already restricted the much wider family of possible deformation modes and thus cannot expect to observe all possible rheological phenomena and behaviors that the material could provide. Other steady deformation modes than simple shear are pure shear, volume changing flows, or mixed-flow, where one can further distinguish between planar flows $S_2^D = 0$ and other, more general flow situations.[19,25,47,50] Nevertheless, the chute flow geometry has advantages, as it allows us to directly observe some non-Newtonian contributions with highly accurate statistics, as will be detailed below.

B. Constitutive model for Newtonian flow

One can decompose the stress into an isotropic and a deviatoric part, ignoring the non-symmetric contribution for the sake of brevity,

$$\boldsymbol{\sigma} = p\mathbf{1} + \boldsymbol{\sigma}^D, \tag{20}$$

where $\boldsymbol{\sigma}^D$ is the (trace-free) deviatoric stress. According to our sign convention, a positive pressure p indicates compression. This is opposite to the convention for strain, such that the first eigenvalues S_1^D and σ_1^D correspond to the compressive deformation direction, and the expected response (a compressive, i.e., positive, stress increase). The deviatoric stress for a Newtonian fluid, denoted by the subscript N, is proportional to the deviatoric strain rate, $\mathbf{S}^D$, and thus satisfies

$$\boldsymbol{\sigma}_N^D = -2\eta_N \mathbf{S}^D, \tag{21}$$

where $\eta_N > 0$ is the (constant) Newtonian shear viscosity.[61] Equation (21) requires that the deviatoric stress tensor and the (negative) strain rate tensor are collinear, i.e., the tensors $-\mathbf{S}^D$ and $\boldsymbol{\sigma}^D$ have the same orientation, or eigensystem.

In the chute flow case, $V_x(z)$ is the only non-zero component of the flow velocity and is monotonically increasing with z, i.e., $\dot{\gamma} = \partial V_x/\partial z \geq 0$. This flow situation is referred to as simple shear for which the deviatoric strain rate tensor is given by a special tensor,

$$\mathbf{S}^D = \frac{\dot{\epsilon}^D}{2}\begin{pmatrix} 0 & 0 & 1 \\ 0 & 0 & 0 \\ 1 & 0 & 0 \end{pmatrix}, \tag{22}$$

with shear rate $\dot{\epsilon}^D = |\dot{\gamma}|$. We will use the special (22) to introduce the (general) representation of the tensor orientations. The deviatoric strain rate tensor $\mathbf{S}^D$ can be expressed in terms of its eigenvalue magnitude, $\frac{\dot{\epsilon}^D}{2}$, representing the magnitude of both the tensile (+) and compressive (−) direction of the strain rate alike, and the orientation angle ϕ_ϵ, see Figure 2, which the negative eigenvalue, S_1^D, has with the horizontal: we define the unit deviator

$$\mathbf{D}(\phi_\epsilon) := \mathbf{R}(\phi_\epsilon) \cdot \begin{pmatrix} 1 & 0 & 0 \\ 0 & 0 & 0 \\ 0 & 0 & -1 \end{pmatrix} \cdot \mathbf{R}^{\mathrm{T}}(\phi_\epsilon) = \begin{pmatrix} \cos^2\phi_\epsilon - \sin^2\phi_\epsilon & 0 & -2\cos\phi_\epsilon \sin\phi_\epsilon \\ 0 & 0 & 0 \\ -2\cos\phi_\epsilon \sin\phi_\epsilon & 0 & \cos^2\phi_\epsilon - \sin^2\phi_\epsilon \end{pmatrix}, \tag{23}$$

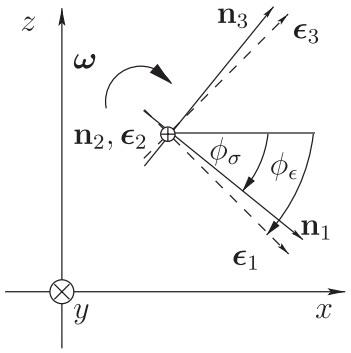

FIG. 2. Sketch of the eigendirections $\mathbf{n}_i$ of the deviatoric stress tensor, the eigendirections $\boldsymbol{\epsilon}_i$ of the strain rate tensor, and the angles ϕ_σ and ϕ_ϵ between the x-axis and the largest (smallest) principal direction of the deviatoric stress (deviatoric strain rate) tensor. Under the assumptions of Sec. IV D, $\mathbf{n}_2 = \mathbf{y}$, while $\mathbf{n}_1$ and $\mathbf{n}_3$ are orthogonal directions in the xz-plane. Thus, the difference between the principal orientation of the negative deviatoric strain rate tensor and the positive deviatoric stress tensor can be quantified by the deviation $\Delta\phi = \phi_\sigma - \phi_\epsilon$.

with the eigenvectors rotated about an angle ϕ_ϵ around the y-axis, i.e., clockwise inside the xz-plane, the superscript T denoting the transpose, and the rotation matrix

$$\mathbf{R}(\phi_\epsilon) := \begin{pmatrix} \cos\phi_\epsilon & 0 & \sin\phi_\epsilon \\ 0 & 1 & 0 \\ -\sin\phi_\epsilon & 0 & \cos\phi_\epsilon \end{pmatrix}. \tag{24}$$

Now we can decompose the deviatoric strain rate tensor $\mathbf{S}^D$, defined in (22), as

$$\mathbf{S}^D = -\frac{\dot{\epsilon}^D}{2}\mathbf{D}(\pi/4) = \frac{\dot{\epsilon}^D}{2}\begin{pmatrix} 0 & 0 & 1 \\ 0 & 0 & 0 \\ 1 & 0 & 0 \end{pmatrix}, \tag{25}$$

with the shear rate $\dot{\epsilon}^D = |\dot{\gamma}|$ and the orientation angle $\phi_\epsilon = \pi/4$. Thus, we expect the deviatoric stress of a Newtonian fluid to satisfy

$$\boldsymbol{\sigma}_N^D = -2\eta_N\mathbf{S}^D = \eta_N\dot{\epsilon}^D\mathbf{D}(\pi/4). \tag{26}$$

Deviations from Newtonian flow rheology can be due to a non-constant viscosity,[51] see below, but also due to an orientation angle of the eigensystem of the stress tensor different from $\pi/4$ – or both together.

C. Non-Newtonian collinear flow for simple shear

For granular flows and other complex fluids (e.g., yield stress fluids), the viscosity is a misleading concept, since it depends on the shear rate and pressure, and since the shear stress can have finite values for $\dot{\epsilon}^D \to 0$, the viscosity diverges in this limit. Therefore, the flow is better described by the macroscopic, bulk friction coefficient μ – referred to as friction μ in the following – which satisfies

$$\boldsymbol{\sigma}^D = -2\mu\frac{p}{\dot{\epsilon}^D}\mathbf{S}^D = \mu\, p\,\mathbf{D}(\pi/4), \tag{27}$$

where p is usually set equal to a measurable stress component, as for example, $p = \sigma_{zz}$, typically perpendicular to the flow direction. Experimentally, the confining stress is often the only measurable stress and, as will be shown below, not equal to the isotropic p.

In other words, stress and strain rate are collinear, but the pre-factor is a function of other variables such as ρ, p, and $\dot{\gamma}$, see the $\mu(I)$ rheology, as discussed in the Introduction. Only for Newtonian fluids one recovers $\mu_N = \eta_N\dot{\epsilon}^D/p$. Because most simple shear element tests involve a confining stress perpendicular to a wall and the corresponding shear stress "along" the wall, the (Cartesian) friction is commonly defined as

$$\mu := -\frac{\sigma_{xz}}{\sigma_{zz}}. \tag{28}$$

This is a misleading and meaningless definition in general flow situations, except for the special case of steady simple shear flow along a wall with normal $\mathbf{z}$. However, it is understandable that it is used so often, since measuring the shear and normal stress on a wall is normally the only way to experimentally access components of the stress tensor.

D. Non-Newtonian flow for simple (plane) shear

In general flow situations, see, for example, Refs. 25 and 47, a decomposition similar to (23) can be formulated for a non-Newtonian stress, where the rotation matrices are replaced by more general transformation matrices between the eigensystems of stress, strain, and the Cartesian laboratory frame. This case will be published elsewhere, and we return to the simple shear in the chute flow geometry which allows us to reduce the three directions to a single variable.

For a symmetric stress, and where the σ_{xy}, σ_{yz} components are close to zero in steady state, the orientation of the deviatoric stress tensor is determined solely by measuring the orientation ϕ_σ of

the largest principal stress in the xz-plane. Then the deviatoric stress takes the form[38]

$$\boldsymbol{\sigma}^D = \mathbf{R}(\phi_\sigma) \cdot \begin{pmatrix} \lambda_1 & 0 & 0 \\ 0 & \lambda_2 & 0 \\ 0 & 0 & \lambda_3 \end{pmatrix} \cdot \mathbf{R}^{\mathrm{T}}(\phi_\sigma), \tag{29}$$

where $\lambda_3 = -\lambda_1 - \lambda_2$. A sketch of this decomposition is presented in Figure 2. Only for the special case of a Newtonian fluid, one would find $\lambda_1 = \eta_N \dot{\epsilon}^D$, $\lambda_2 = 0$, and $\phi_{\sigma,N} = \pi/4$, so that (29) reduces to (21).

The magnitude of friction, deviatoric stress relative to pressure, can be quantified using the tensor-invariant

$$s_D^\star := \frac{1}{\sqrt{6}p}\sqrt{(\lambda_1-\lambda_2)^2 + (\lambda_2-\lambda_3)^2 + (\lambda_3-\lambda_1)^2} \tag{30a}$$

which is the scaled deviatoric norm (a measure of magnitude) of the deviatoric stress tensor. In the collinear (plane strain rate and plane stress) case, one can show that $\mu = s_D^\star$.

Instead of using the third invariant, we further measure how much each principal direction contributes to the deviatoric stress by determining the ratio of the first two eigenvalues,

$$\Lambda_{12} := \lambda_2/\lambda_1. \tag{30b}$$

Finally, in order to obtain an objective, frame-independent constitutive model, the orientation (angles) should only appear as differences (relative transformations),

$$\Delta\phi := \phi_\sigma - \phi_\epsilon. \tag{30c}$$

The three measures (30a)–(30c) are sufficient to quantify the anisotropy of the stress tensor. The deviatoric stress can now be written as

$$\begin{aligned} \boldsymbol{\sigma}^D &= \lambda_1 \mathbf{R}(\phi_\sigma) \cdot \left(\begin{pmatrix} 1 & 0 & 0 \\ 0 & 0 & 0 \\ 0 & 0 & -1 \end{pmatrix} + \Lambda_{12} \begin{pmatrix} 0 & 0 & 0 \\ 0 & 1 & 0 \\ 0 & 0 & -1 \end{pmatrix} \right) \cdot \mathbf{R}^{\mathrm{T}}(\phi_\sigma) \\ &= \frac{s_D^\star\, p}{\sqrt{1+\Lambda_{12}+\Lambda_{12}^2}} \begin{pmatrix} -(1+\frac{\Lambda_{12}}{2})\sin(2\Delta\phi) - \frac{\Lambda_{12}}{2} & 0 & -(1+\frac{\Lambda_{12}}{2})\cos(2\Delta\phi) \\ 0 & \Lambda_{12} & 0 \\ -(1+\frac{\Lambda_{12}}{2})\cos(2\Delta\phi) & 0 & -\frac{\Lambda_{12}}{2} + (1+\frac{\Lambda_{12}}{2})\sin(2\Delta\phi) \end{pmatrix}, \end{aligned} \tag{31}$$

where we used $\cos(2\phi_\sigma) = -\sin(2\Delta\phi)$ and $\sin(2\phi_\sigma) = \cos(2\Delta\phi)$, since $\phi_\epsilon = \pi/4$ in our system. The seemingly more complicated form in the second line of (31) can be advantageous, and will be used in Sec. V. It displays the prefactor $s_D^* p$ (similar to μp in (27)) and a normalized unit-deviator, decomposed into a rotated, planar, and a rotation-invariant axial component (the latter is represented by the diagonal matrix with diagonal values proportional to $(-\Lambda_{12}/2,\ \Lambda_{12},\ -\Lambda_{12}/2)$). Given the identical expressions for $\boldsymbol{\sigma}^D$, in Eqs. (29) and (31), where only different variables are used, it is now straightforward to express, for example, the normal stress differences, the Cartesian stress components,[52] or the Cartesian friction, μ, as functions of the (invariant) pressure and the invariants of the deviatoric stress tensor (30).

V. SIMULATION RESULTS

To obtain detailed information about steady flows, we use the expressions defined in Sec. III. The system is equilibrated for $T = 2000$ time units and then averaged over $\Delta T = 500$, with snapshots taken every $\Delta t_a = t_c/2$. Since the flows are uniform in x and y, we further average analytically over

the chute length $\Delta x = 20$ and width $\Delta y = 10$. The profile of a variable χ is thus defined as

$$\langle\chi\rangle(z) = \frac{1}{(\Delta T/\Delta t_a)\Delta x \Delta y} \sum_{i=0}^{(\Delta T/\Delta t_a)-1} \int_0^{\Delta x} \int_0^{\Delta y} \chi(T + i\,\Delta t_a, x, y, z)\, dy\, dx, \tag{32}$$

with χ any macroscopic field. The macroscopic fields are evaluated for all height-values z between base and surface, with a step size of $\Delta z = 0.05$. In the following, we only show averaged quantities and therefore omit the $\langle\rangle$-brackets.

A. Dependence on the coarse-graining width

The resulting height profiles depend strongly on the coarse-graining width w, which needs to be carefully selected. According to Goldenberg *et al.*,[53] each well-defined macroscopic field should yield a plateau of w-values, where the field values (ideally) do not depend on the coarse-graining width.

Here, we show the existence of two plateaus in the right panel of Figure 3, where the density at selected heights is plotted for a representative system with $\theta = 28^\circ$ and $N = 6000$. A *first plateau* exists, for all heights, in the range $0.0025 \leq w \leq 0.1$. For $w < 0.0025$, statistical fluctuations are strong and longer time-averaging or ensemble-averaging is required to obtain useful data. All other macroscopic fields defined in Sec. III show a similar plateau. We conclude that there is a length scale in the system of much less than a particle diameter, d, where continuum fields for all variables can be defined. On this length scale, layering of the flow can be observed when approaching the base boundary.

Further, as reported earlier in 2D,[54] a second, narrower plateau can be observed for $0.6 \leq w \leq 1$ in the bulk of the flow, further than $2w \approx 2d$ away from the wall. To illustrate the differences, we plot the density as a function of height z for $w = 0.05$ and $w = 1$ in the left panel of Figure 3. When averaging on the particle length scale, oscillations due to layering are smoothed out, and we observe only the large gradients. While the particle-scale density is nearly constant in the bulk, it decays slightly near the base, where the density oscillations are strongest, and decays strongly near the surface, where the pressure approaches zero. The momentum density, velocity, contact stress, and fabric components show the same qualitative behavior.

However, the normal kinetic stress in flow direction, σ^k_{xx}, and therefore the granular temperature, T_g, are strongly scale dependent for $w > 0.1$, with values proportional to w^2 in the bulk, as can be seen in Figure 4. Glasser and Goldhirsch[55] showed that the main scale dependence of the kinetic stress tensor stems from the fact that the fluctuating velocity $\mathbf{v}'_i(t)$ is defined in (11) with respect to the coarse-grained velocity $\mathbf{V}(\mathbf{r}(t), t)$ at position $\mathbf{r}$, and not with respect to $\mathbf{V}(\mathbf{r}_i(t), t)$, at the position of the particle. The latter reference is typically used in kinetic theory, where the fluctuating velocity is defined as

$$\mathbf{v}^\star_i(t) := \mathbf{v}_i(t) - \mathbf{V}(\mathbf{r}_i(t), t)\,. \tag{33}$$

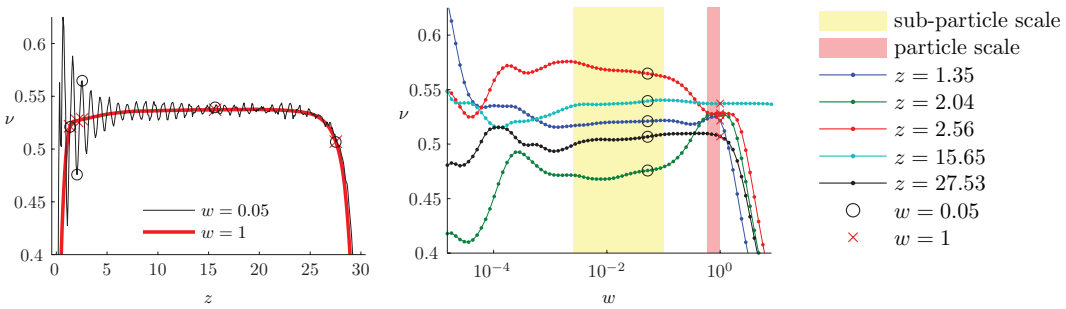

FIG. 3. (Left) Volume fraction as a function of height for $w = 0.05$ and $w = 1$. (Right) Volume fraction at selected heights as a function of the coarse-graining width w. Circles and crosses in both figures denote the density at the selected heights for $w = 0.05$ and $w = 1$, respectively. Data taken for $N = 6000$, $\theta = 28^\circ$.

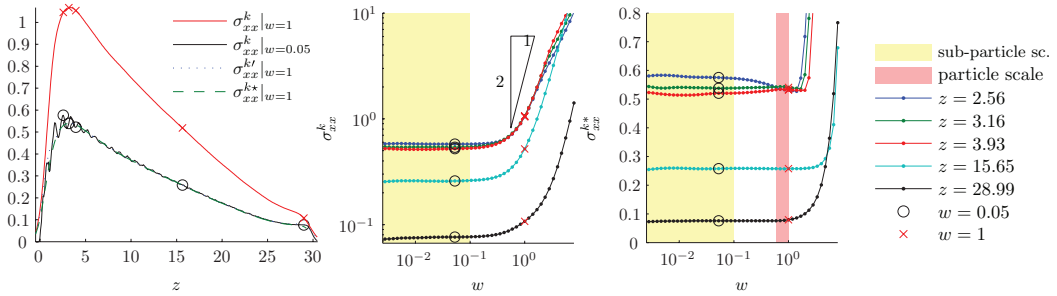

FIG. 4. (Left) Kinetic stress component σ^k_{xx} as a function of height for $w = 0.05$ and $w = 1$, as well as the reduced kinetic stress components $\sigma^{k\prime}_{xx}$ and $\sigma^{k\star}_{xx}$ for $w = 1$. Kinetic stress component σ^k_{xx} (middle) and scale-corrected kinetic stress component $\sigma^{k\star}_{xx}$ (right) at selected heights as a function of the coarse-graining width w. Circles and crosses denote the values at the selected heights for $w = 0.05$ and $w = 1$, respectively.

Kinetic stress components (with contributions from the flow-direction) like σ^k_{xx} can be split into a nearly scale-independent part, $\sigma^{k*}_{xx} = \sum_{i=1}^{N} m v^\star_{ix} v^\star_{ix} \mathcal{W}(\mathbf{r} - \mathbf{r}_i)$, and a scale-dependent part. For large enough samples and in three dimensions, for the coarse graining function used here, the scale-dependent part reduces to $\rho \dot\gamma^2 \frac{w^2}{3}$, which allows us to define a reduced kinetic stress component

$$\sigma^{k\prime}_{xx} = \sum_{i=1}^{N} m v'_{ix} v'_{ix} \mathcal{W}(\mathbf{r} - \mathbf{r}_i) - \rho \dot\gamma^2 \frac{w^2}{3}, \tag{34}$$

where the dominant scale-dependent part has been subtracted. Equation (34) has the advantage that it can be used to correct the stress *a posteriori*, whereas (33) requires a preparation step to obtain $\mathbf{V}$. We confirmed that $\sigma^{k\prime}_{xx}$ is indeed scale independent on both the sub-particle and particle length scale, see Figure 4, and approaches $\sigma^{k\star}_{xx}$. The remaining scale dependence for large w is due to the large macroscopic gradients at the base and the surface. While $\sigma^{k\prime}_{xx}$ does not represent the full kinetic stress component as derived by Goldhirsch,[44] it can be viewed as the scale independent kinetic stress for the particle scale coarse graining. In the following, the reduced kinetic stress is used in all stress calculations for $w = 1$.

As final remark, on the larger coarse-graining length-scale also the granular temperature has to be corrected as $T'_g = (\sigma^{k\prime}_{xx} + \sigma^k_{yy} + \sigma^k_{zz})/(3\rho)$ in (14).

The existence of two plateaus implies two distinct length scales (in this type of flow) and different continuum models should be developed to describe each. Since we are interested in the full details of coarse-grained quantities, we choose $w = 0.05$ as our default coarse-graining width. For coarser continuum modeling, however, the second length scale, $w = 1$, is more appropriate: the details of the layering at the base are not likely to be required to be captured in large-scale continuum models, such as those used to describe geophysical flows.

As an example for the layering, in Figure 5, we study the oscillations in the volume fraction by subtracting the volume fractions ν obtained for the two length scales, at $w = 0.05$ and $w = 1$, and normalizing them by the coarser quantity. These can later be compared to the oscillations found in other macroscopic fields, e.g., stress. The variations due to layering are symmetric about the coarse mean, oscillating periodically, and decaying exponentially with distance from the base, and can be fitted as

$$\tilde\nu = \alpha \cos(2\pi(z - z_w)/L) \exp(-(z - z_w)/z_0), \tag{35}$$

with period $L = 0.907$, first peak within flow $z_w = 1.6$, amplitude at first peak $\alpha = 0.106$, and the $1/e$-decay distance $z_0 = 2.58$. These values are similar for all steady flow simulations; only the decay distance increases for slower flows ($I \leq 0.2$). The period of slightly less than a particle diameter indicates that the particle flow is layered near the base with slightly interlocked layers, even though there is a quite rough wall with roughness of the same order as the layer-distance. Similar

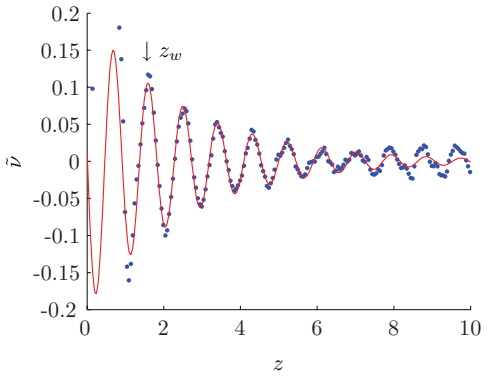

FIG. 5. Dots denote sub-particle-scale variations of the volume fraction, $\tilde{\nu} = \frac{\nu|_{w=0.05} - \nu|_{w=1}}{\nu|_{w=1}}$, as a function of height. The solid line shows the fit to (35), for data taken from the simulation with $N = 6000$, $\theta = 28^\circ$.

variations were also found for micro-fluid flow through a confined nano-channel,[56] but further details go beyond the scope of this study.

B. Continuum conservation equations (coarse grained)

In the steady chute flow situation – not in general – there are some consequences of the macroscopic momentum conservation equations that can be used to check and to better understand the following results.

The horizontal stress components, $\sigma_{\alpha z}$, in dense granular flows are determined by the momentum equations; assuming that the stress is zero at the free surface, and that the flow is steady and uniform, the momentum balance (9) reduces to

$$\sigma_{\alpha z}(z) = \int_z^\infty \left[\rho(z')g_\alpha + t_\alpha(z')\right] dz', \quad \alpha \in \{x, y, z\}, \tag{36}$$

where the boundary interaction force density $\mathbf{t}$, defined in (12), is zero everywhere except within the cutoff distance $c = 2w$ from the basal surface.[9] Equation (36) is called the lithostatic stress relation, since it determines (three) stress components in terms of the density ρ. Since the density is nearly constant, the stress components σ_{xz} and σ_{zz} follow a linear trend, see Figure 6, except for

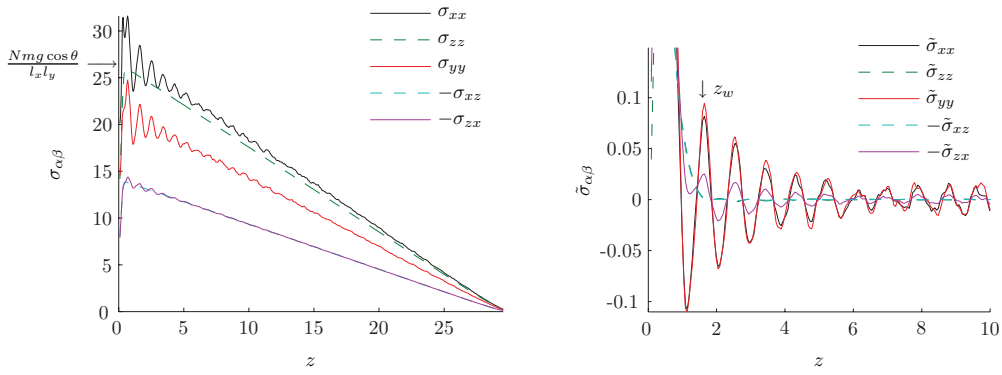

FIG. 6. Total stress components $\sigma_{\alpha\beta}$ (left) for $w = 0.05$ and the sub-particle-scale variations in the stress (right) $\tilde{\boldsymbol{\sigma}} = \frac{\boldsymbol{\sigma}|_{w=0.05} - \boldsymbol{\sigma}|_{w=1}}{\boldsymbol{\sigma}|_{w=1}}$, using the reduced kinetic stress, as defined in (34). Data are taken from a simulation with $N = 6000$ and $\theta = 28^\circ$. Stress components not shown are nearly zero; The normal downward stress, σ_{zz}, increases towards the base, approaching $Nmg\cos(\theta)/(l_x l_y)$, the pressure due to the weight of the flow. In the base regime, the stress decreases to zero, compensated by the boundary interaction force, t_α. Due to the roughness of the base, fluid density and stress do not drop instantly, but over the interval $-1 < z < 1$, see Ref. 9 for details.

small oscillations due to the considerable density oscillations near the base. The oscillations in the remaining stress components, however, are distinctly larger. For example, oscillations in the reduced stress $\tilde{\sigma}_{xx}$ can be fitted (not shown) using Eq. (35), with period $L = 0.900$, $1/e$-decay distance $z_0 = 2.28$, first peak $z_w = 1.63$, and amplitude at first peak $\alpha = 0.0791$. Thus, they are in phase with the density oscillations, suggesting that the stress oscillations are caused by the oscillating density.

Due to the momentum balance (36), both the bulk friction, $\mu = -\sigma_{xz}/\sigma_{zz}$, and the friction due to the interactions with the base, $-t_x/t_z$, are equal to $\tan\theta$ and thus constant for all heights. This is confirmed by our data (not shown).

Further, in all simulations, the stress tensor was found to be nearly symmetric for $w = 1$ (data not shown). In this case, the asymmetric part contributes less than 0.1% to the deviatoric stress with maxima both near the base and the top. For $w = 0.05$, the asymmetric stress is proportional to the density fluctuations and can be larger, but studying this goes beyond the focus of this paper.

Finally, if stress would be isotropic (and symmetric), the normal stress components would be equal. However, the normal stress in flow direction, σ_{xx}, is slightly larger than σ_{zz}, while the normal stress in vorticity direction, σ_{yy}, is smaller, giving rise to non-zero first and second normal stress differences or non-unity stress ratios, as discussed below. In summary, all non-zero stresses that are not governed by the momentum balance (36) show oscillations near the base. These stress oscillations are in phase with the density oscillations shown in Figure 5 and also their period is equal, only the decay distance is slightly smaller, see right panel in Figure 6.

C. Shear rate and inertial number for constant density

Next, we study the shear rate and the inertial number in the chute flow situation, since their behavior is the basis of the $\mu(I)$-rheology, as introduced in Sec. I, and it is at the core of height-averaged macroscopic theories.[39] We define the bulk of the flow to be the region where the $\mu(I)$ rheology is applicable, i.e., where the only control parameter is I, which allows two basic simplifications: In the bulk region (typically ∼80% of the flow if the chute angle is 22° or larger), the density is almost constant and, as definition, the inertial number I is within 10% deviation from its (constant) bulk value, see Figure 7 (right).

Just assuming a constant density $\bar{\rho}$ allows the very simple integration of the steady state momentum balance (36) and yields a linear stress profile $\sigma_{zz} = \bar{\rho} g \cos(\theta)(h_c - z) = \sigma^0_{zz}(1 - z/h_c)$ for $z \in (0, h_c)$, where $\sigma^0_{zz} = \sigma_{zz}(z = 0) = Nmg\cos(\theta)/(l_x l_y)$ is the normal stress (boundary condition) at the base and $h_c = Nm/(l_x l_y \bar{\rho})$ is the height of the flow under the constant density assumption.

Substituting this into the definition of the inertial number, (1), requires a relation between pressure and confining stress $\beta_p = \sigma_{zz}/p$, since in general these stresses are not identical due to

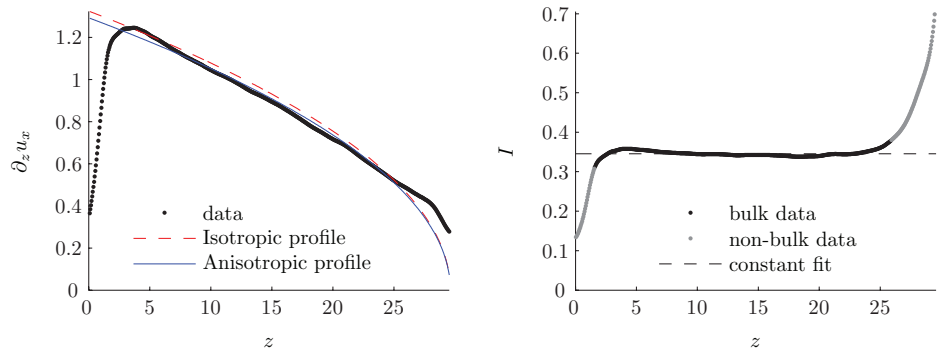

FIG. 7. Shear rate (left) and inertial number (right) plotted as a function of height, for $w = 1$, from the simulation with $\theta = 28°$ and $N = 6000$, In the right figure, we distinguish between bulk data (black markers) and the non-bulk data (gray markers) near the boundaries. The dashed lines show the isotropic Bagnold shear rate profile (37) for constant volume fraction $\bar{\nu} \approx 0.53$ (left panel) and the constant inertial number $\bar{I} = I(28°) = 0.354$ (right panel) as predicted by the $\mu(I)$ rheology, see (41) below. The solid line shows the Bagnold shear rate profile (37) which takes the anisotropy into account.

anisotropy. Further assuming a constant inertial number $\bar{I}$, we obtain the Bagnold shear rate profile

$$\dot{\gamma}(z) = \bar{I}\sqrt{\frac{\sigma_{zz}^0}{\beta_p}\frac{(1 - z/h_c)}{\rho_p d^2}}, \tag{37}$$

which, together with the no-slip condition ($V_x(0) = 0$), yields the Bagnold velocity profile.[57] Now, using the (wrong) isotropy assumption ($\beta_p = 1$) yields the dashed line in Fig. 7, while the proper anisotropy relation ($\beta_p = 1.05$ from (40a) below), yields the solid line. Even though the anisotropy is small it leads to a visible difference in the shear rate profiles.

From the coarse grained data, we estimated the shear rate using centered finite differences,

$$\frac{\partial V_x}{\partial z}(z) \approx \frac{V_x(z + \Delta z) - V_x(z - \Delta z)}{2\Delta z}, \tag{38}$$

with step size $\Delta z = 0.05$. The shear rate predicted in (37) and plotted against the measured shear rate for the reference case in Figure 7, shows that both predictions match the bulk behavior pretty well, but differ significantly near both base and surface: At the base, the shear rate, and thus the inertial number is much lower than predicted. At the free surface, the shear rate decreases but remains finite. Therefore, the inertial number becomes very large at the surface, where the confining stress vanishes.

In summary, the isotropic, collinear $\mu(I)$-rheology predicts the shear rate profile quite well given the crude assumptions about constant density and inertial number. For a better prediction, see Ref. 2, where kinetic theory is used to involve variable density, I, and nonlinear pressure. The theory presented in the following is about the non-isotropic and non-collinear stress contributions and not so much about a slightly improved shear rate profile.

D. Kinetic stress and temperature

Next, we decompose the stress tensor into its kinetic and contact parts. The kinetic stress components are shown in Figure 8. Even for the simulations with high inertial number, as the one shown here with $I \approx 0.25$, the kinetic stresses are much smaller than the contact stresses in the bulk, but significantly contribute to the total stress very close to the surface. Even for the largest $I \approx 0.6$, the kinetic stress is of the order of 10% in the bulk, indicating that its trace, the granular temperature, also has a minor effect. For larger shear rates, lower densities, and pressures, the flow enters the collisional regime where kinetic theory is expected to hold, however, studying this goes beyond the scope of this paper.

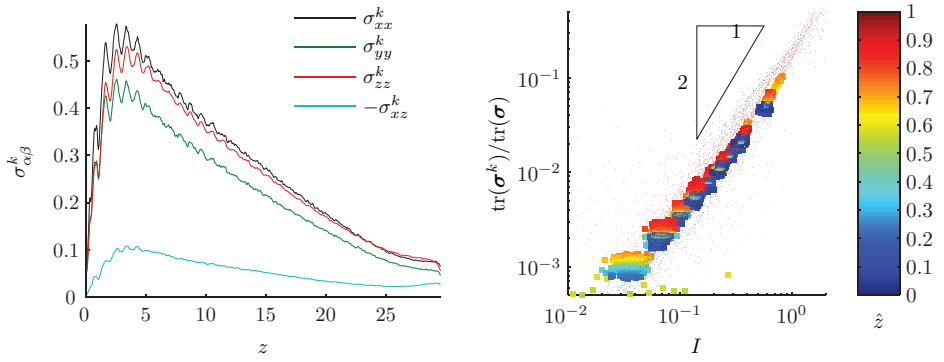

FIG. 8. (Left) Kinetic stress components $\sigma^k_{\alpha\beta}$ for $N = 6000$, $\theta = 28^\circ$, $w = 0.05$. Components not shown are nearly zero. (Right) Ratio of total kinetic pressure to total pressure, $\frac{\mathrm{tr}(\boldsymbol{\sigma}^k)}{\mathrm{tr}(\boldsymbol{\sigma})}$, as a function of inertial number for all data $4000 \le N \le 8000$, $20^\circ \le \theta \le 30^\circ$, $w = 0.05$. Shade/color indicates the relative height, $\hat{z} = z/h$, from darkest gray (blue) at the bottom ($\hat{z} = 0$) to light gray (green/yellow) to mid-gray (red) at the surface ($\hat{z} = 1$). For the height definition, see Weinhart *et al.*[39]

VI. CALIBRATING THE CONSTITUTIVE MODEL

In this section, using the example of steady shear flow, we study the objective descriptors of the stress tensor, as defined in Sec. IV. After splitting off the isotropic part p, the deviatoric stress is expressed in terms of the norm (deviatoric stress ratio) $s_D^\star$, the eigenvalue ratio Λ_{12}, and the orientation of the largest principal component, ϕ_σ. We also examine the contact and kinetic stress contributions $\boldsymbol{\sigma}^c$, $\boldsymbol{\sigma}^k$, as well as the fabric $\mathbf{F}$, for which we use superscripts c, k, F to denote their descriptors.

A. Stress tensor orientation and objective descriptors

From eigenvalue analysis of the deviatoric stress, we obtain its principal directions, or (normalized) eigenvectors, $\mathbf{n}_i$, with the eigenvalues λ_i. The set of eigenvectors allows us to compare the orientation of the stress with the orientation of the strain rate tensor. We confirm the assumptions made in Sec. IV D that the y-components of $\mathbf{n}_1$ and $\mathbf{n}_3$ nearly vanish – except for statistical fluctuations – for strain rate as well as for stress, while $\mathbf{n}_2$ (almost) equals $(0, 1, 0)^T$. Thus, the angle ϕ_σ between the x-axis and the main principal direction, $\mathbf{n}_1$, is the only measurable deviation from a collinear stress-strain relationship.

In Figure 9, the orientation of $\mathbf{n}_1$ is plotted using the angles

$$\alpha_{ab} := -\tan^{-1}\left(\frac{n_{1b}}{n_{1a}}\right), \quad a, b \in \{x, y, z\}, \tag{39}$$

which measure the clockwise rotation angle (around the $b \times a$ axis) in the ab-plane between the a-axis and the projection of $\mathbf{n}_1$ into the ab-plane. As expected, $-\alpha_{xy}$ and α_{zy} nearly vanish. Therefore, the orientation angle of the stress tensor, $\phi_\sigma = \alpha_{xz}$, is slightly below $\phi_\epsilon = 45^\circ$, indicating that the stress tensor is rotated counterclockwise (around the negative y-axis) with respect to the negative strain rate tensor. It is nearly independent of z in the bulk, but oscillates strongly near the base and the difference $|\Delta\phi|$ increases in magnitude closer to the surface.

In the right plot of Figure 9, the eigenvalues of the deviatoric stress tensor are plotted. The second eigenvalue is smallest and negative for all heights and all eigenvalues decrease nearly linearly to zero towards the surface, while their ratios remain nearly constant for all heights, as will be detailed below.

We continue the study of the stress-strain orientation by plotting the angular deviation, $\Delta\phi$, in Figure 10 for all steady simulations. The negative deviation in the bulk increases almost linearly with the inertial number. While the mean bulk deviations are always negative, they oscillate and can become locally positive at low inertial numbers. The linear fit of the deviation angle as a function of inertial number in Figure 11 shows that there is nearly no offset; thus, I and $\phi_\sigma - \phi_\epsilon$ are nearly proportional. However, our data are in a range of $0.02 \leq I \leq 1$, so that the linear fit should not

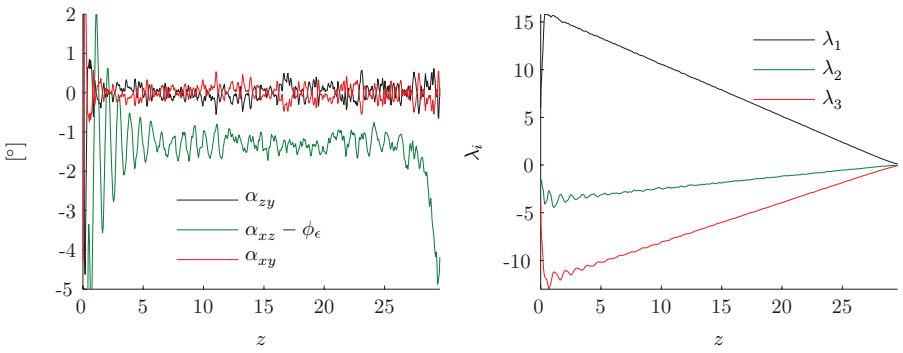

FIG. 9. The deviatoric stress decomposed into principal directions $\mathbf{n}_i$, with corresponding eigenvalues λ_i (right) and α_{xy}, α_{yz}, α_{xz} (left), quantifying the orientation of the eigenvector $\mathbf{n}_1$ as described in the main text. Data are taken from the simulation with $N = 6000$, $\theta = 28^\circ$, and coarse graining width $w = 0.05$.

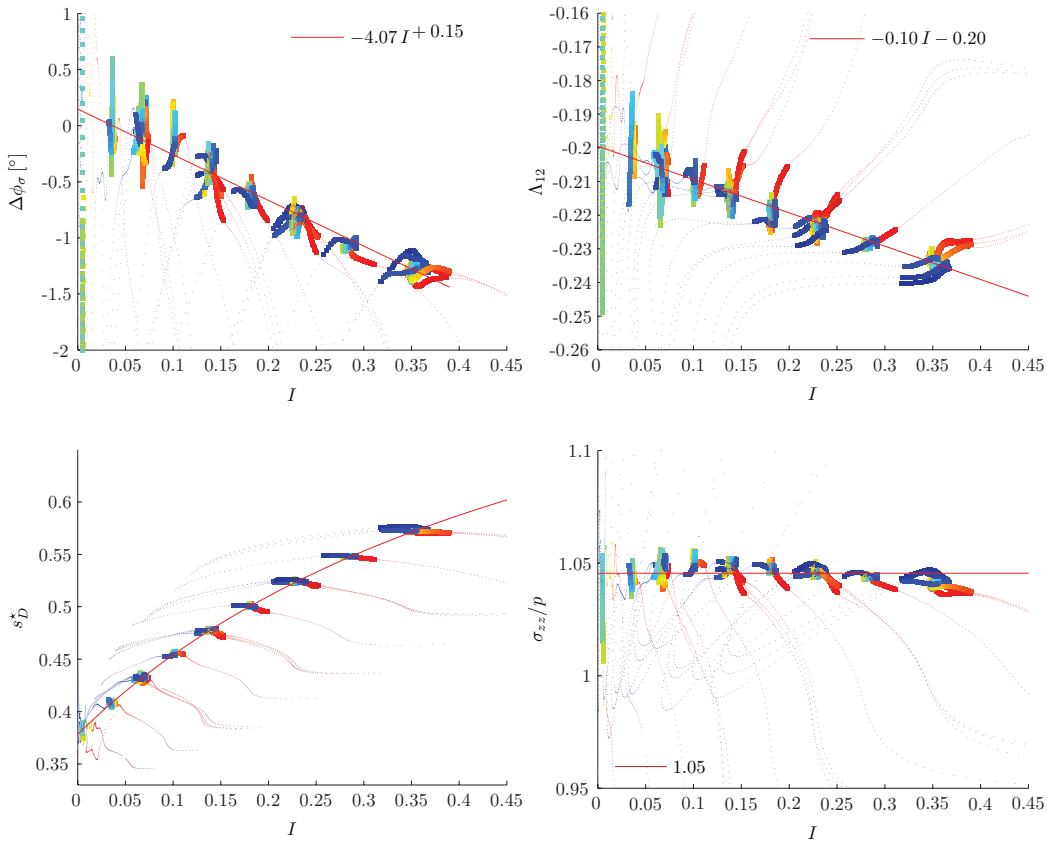

FIG. 10. The four objective variables that describe the stress tensor, one for isotropic pressure and three for the deviatoric stress, are plotted against the inertial number I. Large markers denote bulk values, while small dots denote base and surface values. Shade/color indicates relative height $\hat{z}$ (see Figure 8). Lines indicate fits to the bulk data as specified in the insets. (Top left) Angular deviation of the deviatoric stress from collinearity with the strain rate tensor, $\Delta\phi$, with linear fit (40b). (Bottom left) Magnitude of the deviatoric stress ratio, $s_D^\star$, with the line a fit to the bulk data according to Eq. (40d). (Top right) Ratio of eigenvalues Λ_{12} with linear fit (40c). (Bottom right) Ratio of pressure p and confining stress σ_{zz}, with constant fit. Data are from steady simulations in the parameter range $4000 \leq N \leq 8000$, $20^\circ \leq \theta \leq 28^\circ$, with coarse graining width $w = 1$, using the reduced kinetic stress (34).

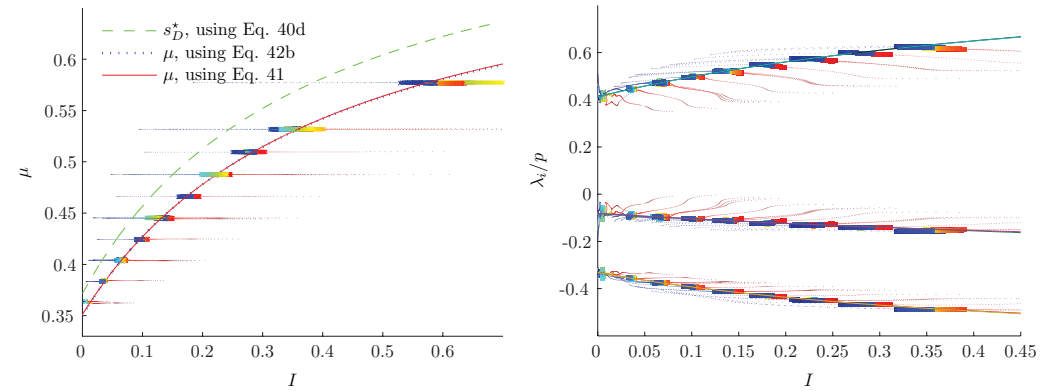

FIG. 11. Friction $\mu = -\sigma_{xz}/\sigma_{zz}$ (left panel) and eigenvalues of the deviatoric stress λ_i scaled by the pressure p (right panel), plotted as function of the inertial number I. Data from various simulations with $4000 \leq N \leq 8000$, $20^\circ \leq \theta \leq 28^\circ$, and $w = 1$, using the reduced kinetic stress (34). The solid lines in each plot are the predictions for μ and λ_i/p, (42), from the (anisotropic) constitutive equations, (40a)–(40d). The dotted line in the left panel is the prediction according to the (isotropic) $\mu(I)$ rheology, (41), the dashed line is the objective friction $s_D^\star$, see (40d).

be extrapolated to either of the large or small I limits without support from more data. Note that a small negative angular deviation corresponds to a positive first (scaled) normal stress difference, $\mathcal{N}_1 = (\sigma_{xx} - \sigma_{zz})/p$, as can be seen from (31). This is in agreement with previous observations, as was reported in the Introduction.

The remaining plots in Figure 10 show the deviatoric stress ratio $s_D^\star$, the eigenvalue ratio Λ_{12}, and the ratio σ_{zz}/p, all plotted as functions of the inertial number I. For each individual simulation with fixed particle number and inclination, in the bulk, the inertial number is (almost) constant and also the plotted values vary only slightly. Deviations from this data-collapse are evident close to the base and the free surface, indicating the limits of the scaling relations. The ratio Λ_{12} is negative throughout, and increases in magnitude with the inertial number, but is finite as $I \to 0$. It is fitted linearly; however, the data do not allow us to conclude about a possible divergence of Λ_{12} for $I \to \infty$. The ratio σ_{zz}/p is independent of the inertial number, with the same reservations outside the range of our data. The fits obtained for $w = 1$ closely match the fits for $w = 0.05$, where the latter display large oscillations close to the base due to the layering (not shown).

Further simulations with a smaller microscopic friction coefficient, $\mu_c = 0.125$, and with no microscopic friction, $\mu_c = 0$, have been analyzed to study the dependence of the angular deviation, $\Delta\phi$, on the microscopic friction. While the magnitude of $\Delta\phi$ decreases with decreasing micro-friction, $\Delta\phi$ remains negative and proportional to I, even for frictionless particles (data not shown) – in the range of data available for steady chute flow.

B. Objective variables as function of inertial number *I*

The fits in Figure 10 can now be used to formulate a constitutive model that allows to reconstruct (predict) the anisotropic and non-collinear stress tensor for a given inertial number: The confining stress σ_{zz} is determined by (36) and depends on the density, which is a function of the inertial number[39] that depends on the chute angle. The pressure shows an almost constant ratio with the confining stress, and the deviatoric stress is given by (31), with

$$p = \sigma_{zz}/\beta_p, \tag{40a}$$

$$\Delta\phi(I) = \Delta\phi_\sigma^0 - \beta_\phi^\sigma I, \tag{40b}$$

$$\Lambda_{12}(I) = \Lambda_{12}^0 - \beta_{12}^\sigma I, \tag{40c}$$

$$s_D^\star(I) = \tan\theta_1^\star + (\tan\theta_2^\star - \tan\theta_1^\star)\frac{I}{I_0^\star + I}, \tag{40d}$$

with coefficients $\beta_p = 1.05$, $\beta_\phi^\sigma = 4.07$, $\Delta\phi_\sigma^0 = 0.15$, $\beta_{12}^\sigma = 0.10$, $\Lambda_{12}^0 = -0.20$, $\theta_1^* = 20.72 \pm 0.01^\circ$, $\theta_2^* = 41.48 \pm 0.06^\circ$, and $I_0^* = 0.568 \pm 0.004$, as shown in Figure 10. Note that all coefficients given in (40a)–(40d) could be functions of the flow variables (e.g., ρ, p, T_g, $\mathbf{F}$); this, however, has not been explored in detail. The first three variables are related in the framework of kinetic theory,[2] while the fabric relates micro-structure to stress, shear rate, and density via (shear) dilatancy and structural anisotropy.[7,46,47,58] The deviatoric fabric – even though correlated to the stress and behaving similarly with respect to anisotropy and non-collinearity with the strain rate – is evolving independent of stress and thus requires a constitutive model of its own, which goes beyond the scope of this study.

Since the objective friction $s_D^\star$ shows a very similar behavior as the Cartesian friction $\mu = -\frac{\sigma_{xz}}{\sigma_{zz}}$, we used the same fit-function for $s_D^\star$ as applied to the friction μ in Ref. 12. This similarity is not surprising as the $\mu(I)$ rheology is a special case of the constitutive model (40a)–(40d) for $\Delta\phi = \Lambda_{12} = 0$ and $\beta_p = 1$. Under these assumptions, $\mu = s_D^\star$ can be fitted well by

$$\mu_{iso}(I) = \tan\theta_1 + (\tan\theta_2 - \tan\theta_1)\frac{I}{I_0 + I}, \tag{41}$$

with fit parameters $\theta_1 = 19.67 \pm 0.01^\circ$, $\theta_2 = 39.89 \pm 0.06^\circ$, and $I_0 = 0.617 \pm 0.004$, as shown in Figure 11.

Note that the $s_D^\star$ norm, which represents the objective deviatoric stress to pressure ratio, similar to a von Mises flow rule, is also a generalized measure of the internal bulk friction in anisotropic flows. Alternative flow rules, like the Lade surface, have been shown to better reproduce the stress response to different strain rate tensors as used here, but since those data are not presented here, we refer from discussing this further for the sake of brevity and rather refer to the recent work of Thornton and Zhang.[5]

C. Consistency check of the model

Next, we confirm that the constitutive model for deviatoric stress is well-posed and consistent. Therefore, the friction μ and the eigenvalues λ_i of the deviatoric stress are plotted and compared with the predictions from the constitutive model in Figure 11.

In particular, the constitutive model (31) predicts that the λ_i depend only on the inertial number I and linearly on the pressure p (note that λ_i is independent of $\Delta\phi(I)$),

$$\lambda_1 = \frac{s_D^\star(I)}{\sqrt{1 + \Lambda_{12}(I) + \Lambda_{12}^2(I)}}\, p\,, \quad \lambda_2 = \Lambda_{12}(I)\,\lambda_1, \quad \lambda_3 = (-1 - \Lambda_{12}(I))\,\lambda_1\,, \tag{42a}$$

as clearly verified in Figure 11 for all bulk data. More interestingly, see (31), the friction factor can be expressed as

$$\mu(I) = \tan(\theta) = -\frac{s_D^\star(\Lambda_{12} + 2)\cos(2\Delta\phi)}{s_D^\star \Lambda_{12} - s_D^\star(\Lambda_{12} + 2)\sin(2\Delta\phi) - 2\sqrt{1 + \Lambda_{12} + \Lambda_{12}^2}}, \tag{42b}$$

which yields for small $\Delta\phi \to 0$ and $I \to 0$

$$\tan(\theta_1) \approx -\frac{(1 + \Lambda_{12}^0/2)}{\Lambda_{12}^0/2 - \sqrt{1 + \Lambda_{12}^0 + (\Lambda_{12}^0)^2}/\tan\theta_1^*}, \tag{43}$$

and thus relates the coefficients of the isotropic and anisotropic constitutive equations, (40a)–(40d) and (41). The friction predicted by inserting the constitutive equations (40a)–(40d) into (42b) agrees very well with the plotted data and also with the direct fit to μ, Eq. (41), for the range of $I < 0.5$, see Figure 11. Ignoring the non-collinearity $\Delta\phi$ leads to deviations already for $I \geq 0.2$ and thus is not desirable for most of the flow conditions studied. Further, the new constitutive stress model allows for the deviatoric stress tensor, Eq. (31), to be anisotropic and the normal stress ratios, such as $K = \sigma_{xx}/\sigma_{zz}$, can be expressed in terms of the inertial number, again inserting Eqs. (40a)–(40d)

$$K(I) = 1 + 2\tan(2\Delta\phi)\mu(I) \tag{44}$$

which compares well with the bulk data (not shown). Isotropy in the shear plane, $K = 1$, follows directly for the collinear case $\Delta\phi = 0$. The (anisotropic) constitutive model (40a)–(40d) yields $K = 0.996$ for $I = 0$. This result is inconsistent with the anisotropic Savage-Hutter model,[32] as presented in Iverson and Denlinger.[59] They defined an earth pressure coefficient as $K = (1 + \sin^2\phi_{int})/(1 - \sin^2\phi_{int})$, with the internal bulk friction angle $\phi_{int} = \tan^{-1}(\mu)$. Our constitutive model is valid in the range of steady state flow angles $\theta_1 < \theta < \theta_2$; for $I \approx 0.35$, as shown in most previous figures as example case, $\theta = 28^\circ$, it predicts $K \approx 1.05$ and $K_y = \sigma_{yy}/\sigma_{zz} \approx 0.81$, clearly different from the isotropic case. The normal stress differences are not discussed here for the sake of brevity, but can be easily extracted from the constitutive model.

D. Objective descriptors of other tensors

Concerning the isotropic components of strain rate and fabric, we just note that the isotropic strain rate vanishes due to the steady flow situation, and the isotropic stress and its relation to the isotropic (trace of) fabric, see Eq. (16), were discussed before for (quasi-)static cases[46,47] and

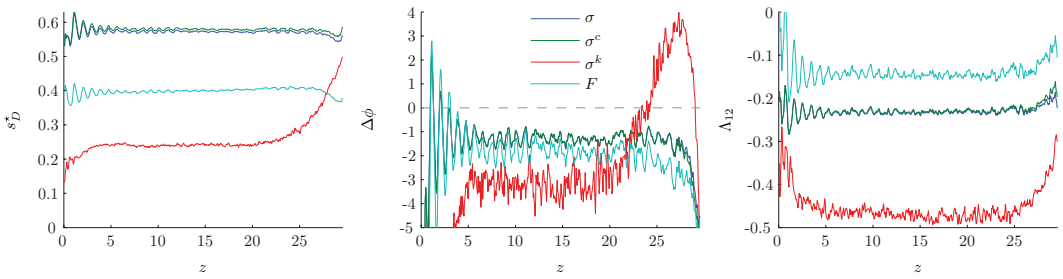

FIG. 12. Decomposition of the symmetric traceless parts of the total, contact, and kinetic stresses and of the fabric tensor, into magnitude $s_D^\star$ (left), angular deviation $\Delta\phi$ (center), and eigenvalue ratio Λ_{12} (right). Data are taken for $N = 6000$, $\theta = 28^\circ$, $w = 0.05$.

dynamic, collisional/inertial flows[2] and therefore will not be detailed further. Finally, we compare the decomposition of the symmetric traceless part of the stress tensor in its objective descriptors with the same objective variables of the contact stress, the kinetic stress, and the fabric tensor in Figure 12. As the contact stress is the dominant component of the stress tensor, even close to the surface, the eigenvalues and principal directions of $\boldsymbol{\sigma}^c$ and $\boldsymbol{\sigma}$ are nearly equal, while $\boldsymbol{\sigma}^k$ shows larger $\Delta\phi$ and a sign change towards the surface. The decomposition of the fabric tensor $\mathbf{F}$ and total stress $\boldsymbol{\sigma}$ are also similar, which is not surprising since these tensors differ only by the weighting of the terms in the summation used to calculate them. The decomposition of $\mathbf{F}$ is nearly constant over the height (and therefore can be described in terms of the inertial number), but the deviation $\Delta\phi$ is stronger for the fabric than for the stress. The magnitude of anisotropy in $\mathbf{F}$ is smaller than in $\boldsymbol{\sigma}$; the angular deviation, however, is stronger. The consequences of the differences between stress and fabric will be discussed in more detail elsewhere.

The kinetic stress is large at the base and decreases towards the surface, see Figure 8. It does, however, not vanish at the surface, unlike the contact stress, and therefore has a larger contribution to the total stress near the surface, in the dilute collisional regime.[2] For all steady cases, the anisotropy in the kinetic stress part alone is smaller than the anisotropy of the contact stress, but is still significant, and even strongly increases towards the surface. The angular deviation $\Delta\phi$ is stronger for the kinetic than for the contact stress: while it remains nearly constant in the bulk, $\Delta\phi$ for the kinetic stress changes sign below the surface and takes much larger negative values towards the base, for all steady flows. These effects occur in a large part of the flow and thus are more than only boundary effects, different from the change in behavior of the contact stress very close to the boundaries.

The data for Λ_{12} show the correlation between the tensor shapes with respect to their non-planar component. The axial (compressive perpendicular to the shear-plane) component of the structural anisotropy is weakest, for the stress it is larger, and for the kinetic stress almost $-1/2$, which is the fully axial limit. In that respect, the kinetic stress is isotropic in the shear-plane, i.e., gas/fluid-like, while the static/contact stress and the structure tensor are behaving similar to each other: their major contribution is responding to the planar strain field while a smaller, second contribution is axial, like the kinetic stress. Since we believe that the full understanding of the non-Newtonian flow behavior can be achieved only by considering all tensor variables together, we end this subsection by including a few data on the correlations between the structure and stress tensor: The isotropic quantities, p and $\mathrm{tr}(\mathbf{F})$, for a given chute angle, scale independent of the filling height, while smaller chute angles correspond to slower flow with larger densities and thus larger $\mathrm{tr}(\mathbf{F})$ at comparable stress levels (data not shown). The anisotropic fabric measures are compared to the corresponding stress measures in Fig. 13:

(1) The non-collinearity, i.e., the angular deviation between fabric/stress and strain rate displays a similar proportionality with I for both tensors. This is not astonishing, since the vorticity ($\omega = \dot{\gamma}/2$ and thus proportional to I, in the plane strain chute flow case) is responsible for different orientations. However, the fabric displays an about 50% larger lag-angle than the stress, indicating a slower relaxation of the structure orientation than of the stress.

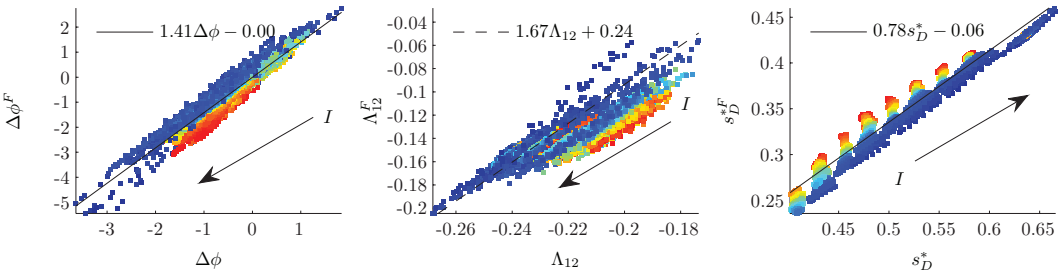

FIG. 13. Correlation's between the objective fabric and stress parameters, for $w = 0.05$, with only the bulk values (∼70% of the flow) shown. (Left) Fabric vs. stress non-collinearity; (center) fabric vs. stress shape; (right) fabric vs. stress "anisotropy"; where the lines in the left and right panels represent fits to all bulk data and the dashed line in the center panel is the fit to all bulk data at inclination $\theta = 28^\circ$. Arrows indicate the direction in which I is increasing.

(2) The tensor-shape Λ_{12}^F does not scale with the stress shape factor; different chute angles correspond to similar slopes ($1.75 - 1.56$) with different offsets ($0.26 - 0.19$) when fitted separately ($\theta \in [28^\circ; 22^\circ]$). The dashed-dotted line shows the fit to the data with $\theta = 28^\circ$; when extrapolated (outside the range of our data) to much larger I, both tensors approach their limits $\Lambda_{12} \approx \Lambda_{12}^F \approx -0.5$, namely, purely axial shape, indicating that the flow response becomes more and more isotropic (tensile) in the shear plane while harvesting a compressive out-of-shear-plane component. The fact that the fabric-shape factor is smaller than the stress-shape factor indicates that the structure is more closely following the planar strain-rate, i.e., the axial out-of-shear-plane compressive contribution is smaller for the fabric.

(3) The tensor "anisotropy" factors, i.e., the ratios of second and first invariants for each tensor, display an almost linear scaling (as indicated by the linear fit (solid line) to all our bulk data). However, in contrast to the stress anisotropy that is almost constant for given θ, the fabric anisotropy systematically increases by about 20%–25% with increasing height z, i.e., with decreasing pressure. This is consistent with observations made in quasi-static pure shear situations for higher densities.[47] Also the fact that the linear fit shows a smaller slope and a negative offset is consistent with those data, as it indicates that fabric becomes isotropic faster than stress, and even could reach zero for finite stress-anisotropy (however, this prediction is again a crude extrapolation outside the range of our data and thus should be treated with care).

In summary, the fabric tensor is a complementary quantity to the stress, with different quantitative and qualitative behavior, resembling the "memory" of the system to previous deformation. Even for the simple steady chute flows considered here, the fabric tensor behaves different from the stress. This indicates that it is the missing link between stress and strain – and thus a missing ingredient for granular rheology – and that the fabric needs objective evolution equations by its own (which is work in progress, based on recent research[5,7,8,18,47,58]).

VII. CONCLUSION

In this paper, discrete particle simulations of dry, frictional, granular flows down a chute, inclined by an angle θ, were studied in the steady state flow regime. The goal was to determine the influence of the local stress anisotropy on the flow rheology and to propose an objective continuum description of the local flow situation that involves all invariant variables – some of which are often neglected.

First, macroscopic fields were obtained by coarse-graining and time-averaging the microscopic data in Sec. V A. Two coarse-graining length scale regimes were identified, for which the bulk macroscopic fields are scale independent, see Figure 3. On the shorter, sub-particle length scale, $0.0025d \leq w \leq 0.1d$, oscillations are visible in the density and stress fields due to the layering of the particles close to the rough base. The oscillations of the macroscopic fields, having a period of

just below one particle diameter, are in phase with each other, and decay away from the boundary, see Figures 5 and 6.

On the longer, particle length scale, $0.6d \leq w \leq d$, smooth macroscopic fields are evidenced. The kinetic stress component in flow direction σ^k_{xx} and the granular temperature T_g were found to be scale-dependent on this scale, see Figure 4. However, the scale-dependence could be clearly quantified as a function of the density and strain rate, which allowed us to obtain a smooth, scale-independent definition of the stress tensor and the granular temperature after removal/subtraction of the coarse-scale dependent term. Note that the second, particle-scale plateau is not defined near the free surface, at the base of the flow, or in general in the presence of large gradients. In these regions, the fields vary on a length scale smaller than or comparable to the used coarse-graining width (due to the large gradients in, e.g., density) so that these results have to be treated with special care.

Next, we considered the three objectives outlined in Sec. I D. The non-Newtonian stress tensor was decomposed into four objective, frame-invariant variables: (i) the objective friction coefficient, $s^\star_D$, very similar to the classical bulk friction, (ii) the anisotropy distribution between the principal axes, Λ_{12}, that describes the "shape" of the stress tensor, (iii) the ratio between pressure p and confining stress, σ_{zz} (in this flow situation), and (iv) the difference in orientation of the stress tensor with respect to the negative strain rate tensor in the shear plane, quantified by one angle $\Delta\phi$.

Each variable was determined in terms of the inertial number, I (see Figure 10), the ratio of the time scale of deformation, $\tau_\gamma = \dot\gamma^{-1}$, and the inertial time scale, $\tau_p = d\sqrt{\rho_p/p}$ (as previously[12] used to describe the bulk flow rheology).

The classical Cartesian bulk friction $\mu = -\sigma_{xz}/\sigma_{zz}$ is well defined and objective only in cases where a plane shear strain rate defines a flow as well as a gradient direction. In the present case, the momentum balance (36) yields $\mu = \tan\theta$ for steady flows. In more general situations, especially in non-planar flows, it is a misleading concept and has to be handled with care. Instead, the ratio of deviatoric norm (second invariant) and pressure is always objective and – in the present case of chute flow – behaves similar as the classical friction, $s^\star_D \propto \mu$, but displays somewhat larger values.

The angular deviation in the shear plane, $\Delta\phi$, was found to be quite small but scales linearly, nearly proportional, with I. In particular, an earlier reported change of sign of $\Delta\phi$ is possible for very small I, but our steady state chute flow provides only intermediate values of I; faster flow accelerates and slower flow arrests.

The "shape" factor Λ_{12} is approximately linear in I with a constant offset, i.e., the stress tensor always has a different shape from the strain rate tensor. Remarkably, $\Lambda_{12}(I \to 0) \neq 0$, if the local system is sheared long enough to reach steady state.

Finally, the ratio σ_{zz}/p was found to be nearly constant, except for the fluctuations in p caused by the layering, when considering the data coarse-grained on the sub-particle scale.

All conclusions are consistent – apart from the oscillations – on both coarse-graining length scales. When ignoring the oscillations, the four constitutive equations (40a)–(40d) allow us to completely determine (re-construct) the Cartesian stress tensor in terms of the inertial number and the confining stress σ_{zz}, which is determined by the momentum balance (36) for steady flows.

Our current steady state stress model predicts a flow rheology (velocity profile and magnitude) very similar to previous models – given the rather small deviations from the original, less general models. The main advantage is that it predicts the full, anisotropic, non-collinear stress; furthermore, we expect that the local, objective, general constitutive model will prove more valuable in different flow situations and especially in dynamic or evolving (non-steady) flows.

Finally, the structural anisotropy was briefly examined. Even though it correlates qualitatively with the deviatoric stress, concerning its dependence on I, it displays different quantitative response to shear, implying that it is an independent state variable that requires a constitutive evolution equation by its own, as proposed in recent studies.[5,7,18,47,58] Taking into account not only the anisotropy of the stress tensor but also the structural anisotropy allows to formulate a local model with the goal to make better predictions of the flow behavior of granular media in general flow situations. Therefore, this paper contributes to the development of objective, inherently anisotropic, local constitutive models – in contrast to non-local models – where the additional internal degree of freedom plays the role of non-local terms, but remains local in essence.

ACKNOWLEDGMENTS

Scientific discussions with M. Liu, E. Clément, and O. Bokhove are gratefully acknowledged.

Financial support by the Deutsche Forschungsgemeinschaft (DFG) Project PiKo 1486 "Sintering – modeling of pressure-, temperature-, or time-dependent contacts" and the NWO STW VICI grant 10828 "Bridging the gap between particulate systems and continuum theory" are acknowledged, as well as the support by the IMPACT-SIP1 project "Computational multi-scale modelling of super-dispersed multiphase flows."

The DPM simulations and the coarse-graining presented in this paper, were undertaken using the open-source Mercury-DPM (www.MercuryDPM.org). It is primarily developed by T. Weinhart, A. R. Thornton, and D. Krijgsman as a joint project between the Multi Scale Mechanics (Mechanical Engineering) and the Mathematics of Computational Science (Applied Mathematics) groups at the University of Twente.

[1] N. Sela and I. Goldhirsch, "Hydrodynamic equations for rapid flows of smooth inelastic spheres, to Burnett order," J. Fluid Mech. **361**, 41–47 (1998).
[2] J. T. Jenkins and D. Berzi, "Kinetic theory applied to inclined flows," Granular Matter **14**, 79–84 (2012).
[3] O. Pouliquen and Y. Forterre, "A non-local rheology for dense granular flows," Phys. Eng. Sci. **367**, 5091–5107 (2009).
[4] K. Kamrin and G. Koval, "Nonlocal constitutive relation for steady granular flow," Phys. Rev. Lett. **108**, 178301 (2012).
[5] C. Thornton and L. Zhang, "On the evolution of stress and microstructure during general 3D deviatoric straining of granular media," Geotechnique **60**, 333–341 (2010).
[6] Y. Jiang and M. Liu, "Granular solid hydrodynamics," Granular Matter **11**, 139–156 (2009).
[7] S. Luding and E. S. Perdahcıoğlu, "A local constitutive model with anisotropy for various homogeneous 2D biaxial deformation modes," Chem.-Ing.-Tech. **83**, 672–688 (2011).
[8] S. Chialvo, S. Jin, and S. Sundaresan, "Bridging the rheology of granular flows in three regimes," Phys. Rev. E **85**, 021305 (2012).
[9] T. Weinhart, A. Thornton, S. Luding, and O. Bokhove, "From discrete particles to continuum fields near a boundary," Granular Matter **14**, 289–294 (2012).
[10] F. da Cruz, S. Emam, M. Prochnow, J.-N. Roux, and F. R. Chevoir, "Rheophysics of dense granular materials: Discrete simulation of plane shear flows," Phys. Rev. E **72**, 021309 (2005).
[11] I. Iordanoff and M. M. Khonsari, "Granular lubrication: Toward an understanding between kinetic and fluid regime," ASME J. Tribol. **126**, 137–145 (2004).
[12] GDR MiDi, "On dense granular flows," Eur. Phys. J. E **14**, 341–365 (2004).
[13] P. Jop, Y. Forterre, and O. Pouliquen, "A constitutive law for dense granular flows," Nature (London) **441**, 727–730 (2006).
[14] Note that the inertial number can also be defined with the bulk density ρ instead of ρ_p and the confining stress σ_{zz} instead of p. All definitions produce equally good fits for the purpose of this paper. This can be contributed to the fact that the ratio σ_{zz}/p turns out to be constant, see Figure 10, while ρ is almost constant in the bulk and furthermore is itself a function of I, see Weinhart *et al.*,[39] and references therein.
[15] I. S. Aranson and L. S. Tsimring, "Continuum description of avalanches in granular media," Phys. Rev. E **64**, 020301 (2001).
[16] L. S. Mohan, K. K. Rao, and P. R. Nott, "A frictional Cosserat model for the slow shearing of granular materials," J. Fluid Mech. **457**, 377–409 (2002).
[17] M. Otsuki, H. Hayakawa, and S. Luding, "Behavior of pressure and viscosity at high densities for two-dimensional hard and soft granular materials," Prog. Theor. Phys. Suppl. **184**, 110–133 (2010).
[18] J. Sun and S. Sundaresan, "A constitutive model with microstructure evolution for flow of rate-independent granular materials," J. Fluid Mech. **682**, 590–616 (2011).
[19] C. H. Rycroft, K. Kamrin, and M. Z. Bazant, "Assessing continuum postulates in simulations of granular flow," J. Mech. Phys. Solids **57**, 828–839 (2009).
[20] R. M. Nedderman, *Statics and Kinematics of Granular Materials* (Cambridge University Press, Cambridge, 2005).
[21] I. Vardoulakis and J. Sulem, *Bifurcation Analysis in Geomechanics* (Chapman & Hall, London, 1995).
[22] P. A. Vermeer, "Non-associated plasticity for soils, concrete and rock," in *Physics of Dry Granular Media*, NATO ASI Series E 350, edited by H. J. Herrmann, J. P. Hovi, and S. Luding (Kluwer Academic Publishers, Dordrecht, 1998), p. 163.
[23] As convention, in the following, we refer to tensors (stress or fabric) as "anisotropic" if their deviatoric part is non-zero. This also involves cases with vanishing normal stress-differences in the Cartesian coordinate system, but with non-vanishing eigen-value differences (second deviatoric tensor invariant) in their eigen-system.
[24] S. Luding, M. Lätzel, W. Volk, S. Diebels, and H. J. Herrmann, "From discrete element simulations to a continuum model," Comput. Methods Appl. Mech. Eng. **191**, 21–28 (2001).
[25] S. Luding and F. Alonso-Marroquín, "The critical-state yield stress (termination locus) of adhesive powders from a single numerical experiment," Granular Matter **13**, 109–119 (2011).
[26] D. Bi, J. Zhang, B. Chakraborty, and R. P. Behringer, "Jamming by shear," Nature (London) **480**, 355–358 (2011).
[27] N. A. Clark and B. J. Ackerson, "Observation of the coupling of concentration fluctuations to steady-state shear flow," Phys. Rev. Lett. **44**, 1005–1008 (1980).
[28] S. Hess, "Shear-flow-induced distortion of the pair-correlation function," Phys. Rev. A **22**, 2844–2848 (1980).
[29] S. Hess, "Shear-flow induced distortion of the radial distribution function, test of a model kinetic equation in the nonlinear flow regime," Physica A **118**, 444 (1983).

[30] S. Hess, "Similarities and differences in the nonlinear flow behavior of simple and of molecular liquids," Physica A **118**, 79–104 (1983).
[31] S. Hess and H. J. M. Hanley, "Pressure tensor and viscosity coefficients of a soft sphere liquid under shear," Int. J. Thermophys. **4**, 97–114 (1983).
[32] S. B. Savage and K. Hutter, "The motion of a finite mass of material down a rough incline," J. Fluid Mech. **199**, 177–215 (1989).
[33] S. Jin and M. Slemrod, "Regularization of the Burnett equations for rapid granular flows via relaxation," Physica D **150**, 207–218 (2001).
[34] M. Alam and S. Luding, "Rheology of bidisperse granular mixtures via event-driven simulations," J. Fluid Mech. **476**, 69–103 (2003).
[35] M. Alam and S. Luding, "Non-Newtonian granular fluids: Simulation and theory," in *Powders and Grains 2005*, edited by R. Garcia-Rojo, H. J. Herrmann, and S. McNamara (Balkema, The Netherlands, 2005), p. 1141.
[36] E. Couturier, F. Boyer, O. Pouliquen, and E. Guazzelli, "Suspensions in a tilted trough: Second normal stress difference," J. Fluid Mech. **686**, 26–39 (2011).
[37] F. Boyer, O. Pouliquen, and E. Guazzelli, "Dense suspensions in rotating-rod flows: Normal stresses and particle migration," J. Fluid Mech. **686**, 5–25 (2011).
[38] R. Hartkamp, A. Ghosh, T. Weinhart, and S. Luding, "A study of the anisotropy in a fluid confined in a nanochannel," J. Chem. Phys. **137**, 044711 (2012).
[39] T. Weinhart, A. Thornton, S. Luding, and O. Bokhove, "Closure relations for shallow granular flows from particle simulations," Granular Matter **14**, 531–552 (2012).
[40] S. Luding, "Cohesive, frictional powders: Contact models for tension," Granular Matter **10**, 235–246 (2008).
[41] L. E. Silbert, D. Ertas, G. S. Grest, T. C. Halsey, D. Levine, and S. J. Plimpton, "Granular flow down an inclined plane: Bagnold scaling and rheology," Phys. Rev. E **64**, 051302 (2001).
[42] L. Lucy, "A numerical approach to testing the fission hypothesis," Astron. J. **82**, 1013–1024 (1977).
[43] Note that the standard deviation of the 3D-Lucy function is equal to its width w, whereas the standard deviation of the 3D-Gaussian[9] of width w is $\sqrt{3}w$; thus, a Lucy coarse-graining function with width w has the same standard deviation as a Gaussian coarse-graining function with width $w/\sqrt{3} \approx 0.58w$.
[44] I. Goldhirsch, "Stress, stress asymmetry and couple stress: From discrete particles to continuous fields," Granular Matter **12**, 239–252 (2010).
[45] C. Goldenberg and I. Goldhirsch, "Continuum mechanics for small systems and fine resolutions," in *Handbook of Theoretical and Computational Nanotechnology* (American Scientific Publishers, Stevenson Ranch, CA, 2006), pp. 330–386.
[46] F. Göncü, O. Duran, and S. Luding, "Constitutive relations for the isotropic deformation of frictionless packings of polydisperse spheres," C. R. Mec. **338**, 570–586 (2010).
[47] O. I. Imole, N. Kumar, V. Magnanimo, and S. Luding, "Hydrostatic and shear behavior of frictionless granular assemblies under different deformation conditions," KONA Powder Part. J. **30**, 84–108 (2013).
[48] All other rank-2 tensors are decomposed in the same spirit, but for the sake of brevity we skip the discussion here and only give the results later, when the data are shown.
[49] In this study, we use the ratio of second and first eigenvalue, where the sorting convention has to be specified for each tensor. The same information is, for example, contained in the Lode angle[5] that is defined as $\tan\alpha_S = (\sqrt{3}(S_2^D - S_3^D))/(2S_1^D - S_2^D - S_3^D) = (1/\sqrt{3})(1 + 2\xi_S)$, with $\xi_S = S_2^D/S_1^D$. In particular, for the chute flow geometry used in this study, one has $\xi_S = 0$ and thus $\alpha_S = 30^\circ$.
[50] C. Thornton, "Quasi-static simulations of compact polydisperse particle systems," Particuology **8**, 119–126 (2010).
[51] R. Hartkamp, P. J. Daivis, and B. D. Todd, "Density dependence of the stress relaxation function of a simple fluid," Phys. Rev. E **87**, 032155 (2013).
[52] Note that the non-diagonal stresses from the data also involve an anti-symmetric stress, $\sigma^A = (\sigma_{xz} - \sigma_{zx})/2$, which has to be considered for the mathematically correct computation of the Cartesian components, i.e., $\sigma_{xy} = -(1 + \frac{\Lambda_{12}}{2})\cos(2\Delta\phi) + \sigma^A$, but which is ignored in the following – for the sake of brevity – since it is rather small, i.e., $\sigma^A/p \ll 10^{-3}$ except at the bottom and at the free-surface (data not shown).
[53] C. Goldenberg, A. Atman, P. Claudin, G. Combe, and I. Goldhirsch, "Scale separation in granular packings: Stress plateaus and fluctuations," Phys. Rev. Lett. **96**, 168001 (2006).
[54] M. Lätzel, S. Luding, and H. J. Herrmann, "Macroscopic material properties from quasi-static, microscopic simulations of a two-dimensional shear-cell," Granular Matter **2**, 123–135 (2000).
[55] B. J. Glasser and I. Goldhirsch, "Scale dependence, correlations, and fluctuations of stresses in rapid granular flows," Phys. Fluids **13**, 407 (2001).
[56] R. Hartkamp and S. Luding, "A continuum approach applied to a strongly confined Lennard-Jones fluid," in *Proceedings of the Fifth International Conference on Multiscale Materials Modeling (MMM2010), Freiburg, Germany* (Brsg Fraunhofer IWM, Freiburg, 2010).
[57] R. A. Bagnold, "Experiments on a gravity-free dispersion of large spheres in a Newtonian fluid under shear," Proc. R. Soc. London, Ser. A **225**, 49–63 (1954).
[58] V. Magnanimo and S. Luding, "A local constitutive model with anisotropy for ratcheting under 2D axial-symmetric isobaric deformation," Granular Matter **13**, 225–232 (2011).
[59] R. M. Iverson and R. P. Denlinger, "Flow of variably fluidized granular masses across three-dimensional terrain. 1. Coulomb mixture theory," J. Geophys. Res. **106**, 537–552, doi:10.1029/2000JB900329 (2001).
[60] A. R. Thornton, T. Weinhart, S. Luding, and O. Bokhove, "Friction dependence of shallow granular flows from discrete particle simulations," Eur. Phys. J. E **35**, 127 (2012).
[61] R. Hartkamp, B. D. Todd, and S. Luding, "A constitutive framework for the non-Newtonian pressure tensor of a simple fluid under planar flows," J. Chem. Phys. **138**, 244508 (2013).